UNIVERSITÀ DEGLI STUDI DI PALERMO

PhD Course - Energy

Engineering Department

The Interaction between Space Charge Dynamics and Partial Discharge Activity in HVDC Cables: Diagnostic Techniques and Advanced Analysis

PhD Student

Ing. Alessio Di Fatta

Supervisor

Prof. Pietro Romano

PhD Program Coordinator

Prof.ssa Eleonora Riva Sanseverino

Co-Supervisor

Ing. Antonino Imburgia

XXXVIII CYCLE

ACADEMIC YEAR 2025 - 2026

Contents

Chapter 1

Introduction

1.1 Context and Motivation

Today, the global energy scenario is under radical changes driven by the need to achieve a more sustainable and efficient power system. This transition is motivated by the goal of mitigating climate change through the large scale integration of renewable energy sources, and it represents a major challenge for the current century [1]. In technical terms, the worldwide electrical grid is evolving from one based on centralized fossil fuel generation to a more complex architecture incorporating decentralized and intermittent sources like wind and solar. In this context, High Voltage Direct Current (HVDC) technology has emerged as a cornerstone to implement this process. Its inherent advantages over traditional High Voltage Alternating Current (HVAC) systems, such as reduced transmission losses over long distances and the ability to interconnect asynchronous grids, make it an indispensable technology for the future of energy transmission [2, 3]. With the spread of HVDC systems, particularly those using extruded polymeric cables for underground and submarine transmission lines, ensuring their long term reliability and operational performance has become a key engineering issue. The reliability of these advanced cable systems is fundamentally dependent on the health state of the electrical insulation. While traditional HVDC systems have historically used mass-impregnated (MI) paper insulation, the industry has recently been moving towards polymeric materials, which represent an alternative that is easier to produce [4]. Among these, Cross-Linked Polyethylene (XLPE) is widely adopted due to its good dielectric, thermal and mechanical properties [5]. However, under the unique stresses of DC operation, these materials are susceptible to degradation mechanisms that can compromise their performance and ultimately lead to premature failure. Therefore, a deep understanding of these aging phenomena is essential for optimizing insulation design, developing robust qualification protocols, and enhancing the overall lifetime of HVDC cable systems.

1.2 The Challenges of HVDC Cables

Unlike in AC systems where the electric field distribution is governed by the permittivity of the dielectric, in DC systems it is influenced by its conductivity. This parameter is highly sensitive to temperature and the local electric field, leading to a non linear and dynamic field distributions under operating loads [6, 7]. These dynamic fields can induce localized stress concentrations, which in turn may trigger aging mechanisms within the insulation. Among the phenomena that influence and are simultaneously influenced by this behaviour are the accumulation of spatial charge and the triggering of partial discharges. Considering the cable system, a brief description of the two phenomena is provided below.

Space charge is an accumulation of electric charges within the bulk of the dielectric material or at the interfaces with the semiconducting layers (semicon) [8]. These charge regions, which can originate from electrode injection or internal ionization, significantly distort the local electric field from its steady state distribution. The process can lead to an enhancement of the localized electric stress, which in turn accelerates material aging and can trigger other degradation mechanisms. Consequently, the accurate measurement and analysis of space charge dynamics are paramount for assessing the performance of HVDC cable.

Partial Discharges (PDs) are small electrical discharges that occur in localized regions of an insulation system where the electric stress exceeds the local dielectric strength [9, 10]. While PDs are a well know phenomenon in AC systems, their behavior under DC stress is more complex and less predictable. In this field, one of the most important aspects is the problem of recognizing and classifying the different nature of PD. In HVDC cables, PD activity is often linked to the presence of manufacturing defects such as voids, contamination, or imperfections at the dielectric/semicon interfaces. Although the phenomenon itself is not destructive, it has been widely demonstrated that its evolution over time systematically leads to failures. For this reason, PD monitoring is of primary importance, as it serves as a direct indicator of ongoing degradation processes.

1.3 Thesis Objectives

Even though they have been traditionally studied as separate issues, space charge accumulation and PD activity are not independent phenomena. Instead, they are intrinsically linked in a dynamic interaction that governs the health status of HVDC insulation. The core hypothesis of this thesis is that the accumulation of space charge can be a primary driver of PD inception and evolution in HVDC cables under operating conditions. Specifically, this work demonstrates that the dynamic distortion of the electric field, caused by space charge accumulation under combined thermal and electrical stresses, can lead to localized regions of high electric stress. When these regions coincide with pre-existing defects, the local field can exceed the discharge inception threshold, triggering PD activity. This thesis provides direct experimental evidence of this causal link, showing that the intensification of PD is not merely a function of the applied voltage, but is critically dependent on the transient behavior of the electric field profile.

1.4 Research Contributions

To validate the central hypothesis and to gain a deeper understanding of the main challenges of HVDC systems, during the three years of Ph.D. activity the following contributions have been made:

Development of an advanced system for space charge measurement. This objective went beyond the use of existing techniques and involved the complete development and validation of an integrated diagnostic system. Key contributions include:

- The successful application of a novel, Pulsed Electro-Acoustic (PEA) cell, developed within the research group of the L.E.PR.E. Lab. of the university of Palermo, which incorporates the latest scientific optimizations for enhanced signal quality on thick insulation cables.
- The development of a custom software in a commercial programming environment, featuring a Graphical User Interface (GUI), to control both the signal acquisition and the entire multi-step signal processing pipeline.
- The validation and deployment of this integrated system, first in a controlled laboratory environment on mini cables, and subsequently in industrial setup for on-site

measurements on full-size 525 kV HVDC cables. This activity has been carried out in collaboration with Prysmian.

Proposal for innovative data analysis methodologies. A primary goal was to improve the accuracy and interpretation of diagnostic measurements by creating new analysis tools. This involved two main areas of innovation:

- The definition of a statistical framework for assessing electric field stabilization. This method uses high frequency data acquisition and statistical trend analysis to provide a more robust, sensitive, and efficient evaluation than the conventional spot check approach.

- The development of advanced clustering algorithms for the separation of PD sources in DC application. By replacing the traditional distance based metric with one based on waveform cross-correlation, these algorithms overcomes the key limitations of standard methods, allowing for the accurate separation of overlapping PD patterns with different shapes and densities.

Experimental investigation of the direct interaction between space charge dynamics and PDs inception. The final objective was to provide definitive experimental proof of the interaction between the two key phenomena. This was achieved by:

- Designing and executing a series of experiments to isolate the effect of operational stresses, such as thermal gradients, on PD activity.

- Conducting a simultaneous measurement of space charge (via PEA) and PDs on a loaded HVDC model cable. This allowed for the direct, time resolved correlation of the electric field evolution with the onset and intensity of PD activity, thereby establishing a clear and quantifiable causal link between space charge induced field inversion and the PDs triggering.

1.5 Thesis Outline

This thesis is structured into six chapters, each building upon the last to construct a comprehensive investigation.

Following this introduction, Chapter 2 provides a detailed overview of the technique used for space charge measurement. It describes the entire diagnostic chain, from the physical principles of the Pulsed Electro-Acoustic (PEA) method and the developed experimental setup, to the multi-step signal processing pipeline required to ensure data fidelity. A significant focus is placed on a comprehensive review and comparative analysis of several signal deconvolution techniques, highlighting their respective strengths and limitations.

Chapter 3 introduces a novel statistical methodology for assessing the stabilization of the electric field within the insulation. This chapter presents a robust alternative to the standard IEEE 1732 procedure, demonstrating how high frequency data acquisition combined with statistical trend analysis can provide a more sensitive, reliable, and efficient evaluation of the stress to which the insulation is subjected.

Chapter 4 addresses the significant challenges of PD analysis in the DC domain. It presents novel, unsupervised algorithms developed to overcome the limitations imposed by the absence of a phase reference. The core of this chapter is the introduction of an advanced clustering method based on waveform cross-correlation for signal separation, complemented by a short comparative review of dimensionality reduction techniques for effective data visualization.

Chapter 5 presents the final experimental work of this thesis, providing direct, quantitative evidence of the interaction between space charge dynamics and PD inception. This chapter details the results of two key investigations: one isolating the effect of thermal gradients on PD activity, and a second, definitive experiment involving the simultaneous measurement of space charge and PD on a loaded model cable, which establishes a clear causal link between the two phenomena.

Chapter 6 summarizes the key scientific contributions of this research. It synthesizes the findings into a cohesive overall conclusion that reinforces the central hypothesis and discusses its implications for the reliability of HVDC systems. The chapter concludes by suggesting several promising directions for future work.

Chapter 2

Advanced Space Charge Measurement using the Pulsed Electro-Acoustic (PEA) Method

2.1 The Space Charge Phenomenon

As mentioned in the introduction, the behavior of dielectric materials under DC stress is fundamentally different from that under AC conditions [5]. While in AC systems the electric field distribution is primarily governed by the material's permittivity, in DC steady-state conditions it is dictated by its electrical conductivity (σ), which depends on temperature (T) and the electric field itself (E), as shown in the following empirical equation [11, 12]:

$$\sigma(T, E) = \sigma_0 \cdot e^{[a(T-T_0)+b(E-E_0)]} \tag{2.1}$$

where σ_0 is the insulation conductivity at reference temperature, T_0 (20°C), and reference electric field, E_0 (usually 0 kV/mm). The coefficients a and b are, respectively, the thermal and electrical dependence coefficients for the conductivity. This distinction is the root cause of many of the unique challenges associated with HVDC cables. Under isothermal conditions and in the absence of load, following the voltage application the distribution of the electric field in the cable is capacitive, with a hyperbolic trend that concentrates the maximum stress near the conductor, as described by the following equation [13]:

$$E(r) = \frac{V_{DC}}{r \cdot \ln(\frac{r_{outer}}{r_{inner}})} \tag{2.2}$$

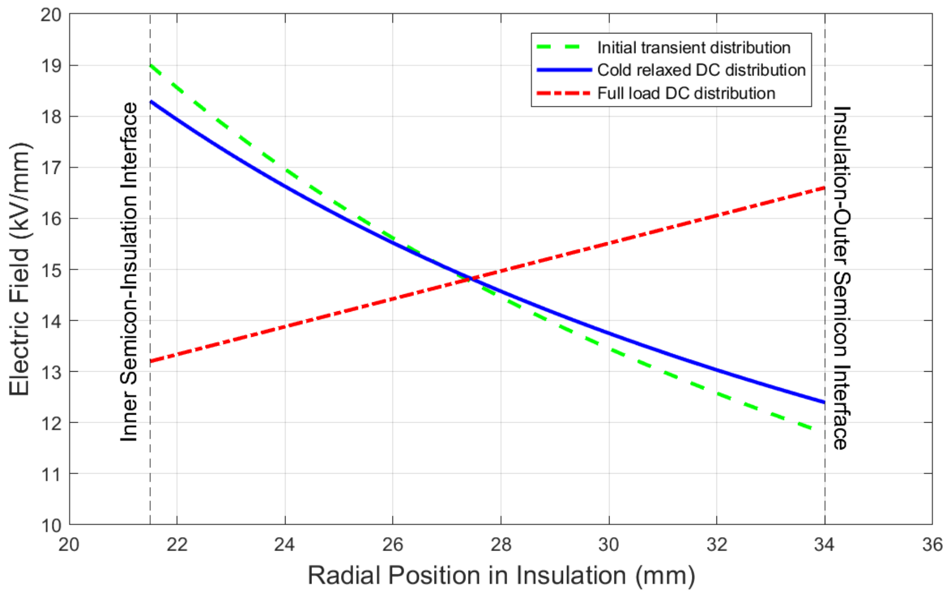

Figure 2.1: Electric Stress Distribution in HVDC Cable Insulation.

where $E(r)$ is the radial electric field at a distance r from the cable axis, V_{DC} is the applied DC voltage, r_{inner} and r_{outer} are the radius of the inner and outer semicon/dielectric interfaces, and r represents the radial position within the insulation layer, with $r_{inner} \leq r \leq r_{outer}$. Subsequently, in steady state and still under no load, the field redistributes according to the conductivity of the insulator, which in turn depends on the local electric field. This implies an increase in conductivity in the inner zone of the dielectric and, therefore, a slight reduction in electrical stress. As shown in Fig. 2.1, the thermal gradient established by the load current is particularly critical because it can lead to a phenomenon known as field inversion, where the region of maximum electric stress shifts from the inner radius (near the conductor) to the outer radius of the insulation, an area that is not designed to withstand such high stress [12]. The field inversion, combined with local distortions caused by the presence of charge in the dielectric bulk or at the interfaces, generates a highly distorted electric field profile. One of the main mechanisms contributing to charge accumulation under DC voltage is interfacial polarization, also known as the Maxwell-Wagner (MW) effect [14, 15]. Practical polymer insulation systems are never perfectly homogeneous, they contain microscopic variations in their structure (crystalline and amorphous regions), chemical impurities and additives. When a DC electric field is applied, free charges move through the material according to local conductivity. In regions with discontinuities with different electrical properties, these charges can accumulate. This process creates localised pockets of charge, distorting the macroscopic electric field. Beyond MW polarization, two other significant mechanisms contribute to the formation of space charge in HVDC cables:

Charge Injection from Electrodes: At the high electric fields present at the interfaces between the semiconducting layers and the dielectric, charge carriers can be injected directly into the insulation material. The intensity of this phenomenon, known as Schottky injection, is determined by the electronic affinity of the materials that make up the interface [16, 17].

Internal Ionization: Charges can also be produced within the bulk of the insulation through the dissociation of impurities or molecules under high electrical and thermal stress [18, 19]. In polymeric materials such as XLPE, residual impurities, additives, or structural defects can ionize or dissociate, creating free charges that either migrate according to local conductivity or become trapped in bulk defects. Elevated temperature enhances charge mobility and dissociation rates, increasing space charge accumulation.

The resulting charge distribution can be classified into two types. Homocharge refers to the accumulation of charges with the same polarity as the adjacent electrode (e.g., negative charges near the cathode). This type of charge tends to reduce the electric field at the interface, acting as a shield. Conversely, heterocharge consists of charges with the opposite polarity to the adjacent electrode (e.g., positive charges near the cathode), which significantly enhances the local electric field. The net effect of these accumulated charges is a significant distortion of the electric field as shown in Fig. 2.2. This distortion can lead to severe localized stress enhancement, which in turn accelerates the material degradation processes and can compromise the dielectric strength of the cable. The dynamics of space charge are further complicated by the cable's operating conditions. Therefore, the accurate measurement of the space charge profile is an essential diagnostic tool for understanding insulation behavior, validating material performance, and ultimately optimizing the design of reliable HVDC cable systems.

2.2 The PEA Method

Among the several techniques available for space charge measurement, the Pulsed Electro-Acoustic (PEA) method is one of the most widely adopted and effective [20, 21]. Historically, the method has been primarily employed on flat dielectric specimens or on model cables with reduced cross-sections compared to practical applications [22, 23]. In view of the increasing interest in charge accumulation dynamics and their influence on cable performance, advanced

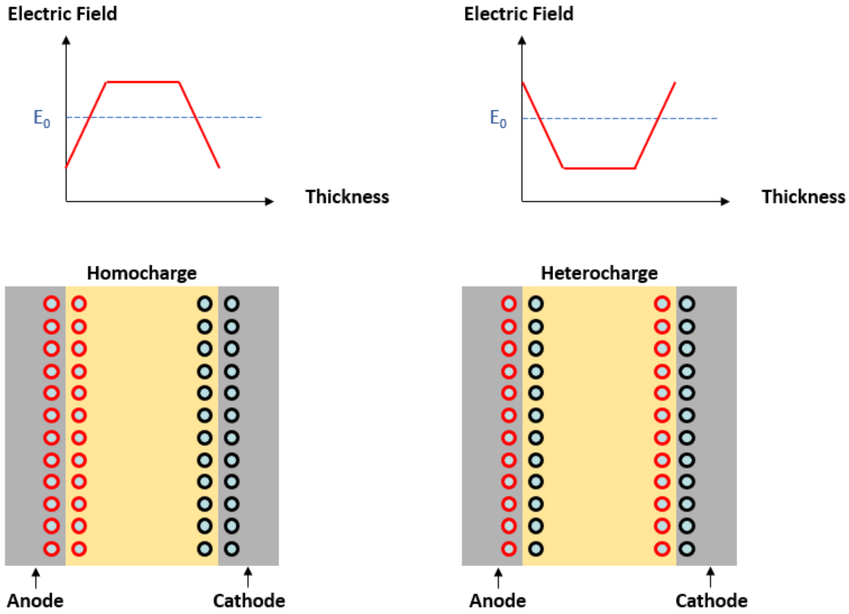

Figure 2.2: Example of homocharge (left) and heterocharge (right) accumulation and their effect on the electric field profile in the case of flat specimens.

variants of the PEA technique have been developed to allow charge measurements on full-size cables [24, 25, 26]. The fundamental principle of the PEA method, a diagram of which is shown in the Fig. 2.3, is the detection of acoustic pressure waves generated by the interaction between accumulated space charges and an externally applied voltage pulse. The measurement process can be summarized as follows: An HVDC voltage (V_{DC}) is applied to the sample, establishing an internal charge distribution. Short duration, high voltage pulses (e_p), in the nanosecond range, are superimposed on the DC voltage. The impulsive electric force causes the charges within the dielectric to vibrate, generating acoustic pressure waves proportional to the local charge density. These waves propagate through the insulation and are detected by a piezoelectric transducer, typically Polyvinylidene Fluoride (PVDF), located on the ground electrode. The transducer converts the pressure signal into a voltage signal (v_{out}), which is then amplified and recorded by an oscilloscope. This signal appears as two voltage peaks representing the charge distributions at the two interfaces, separated in time by an interval that depends on the characteristics of the dielectric (material and thickness) and the applied pulse. The resulting waveform provides a time domain representation of the charge distribution across the insulation thickness. It should be noted that the diagram in Fig. 2.3 is intended for conceptual illustration only. Further details regarding the cell design can be found in [21]. In the case of HVDC cables, the PEA method is adapted using a configuration that allows the pulse to be applied and the acoustic wave to be detected through the cylindrical surface of the sample [26]. Traditionally, a curved electrode wrapped around the cable and

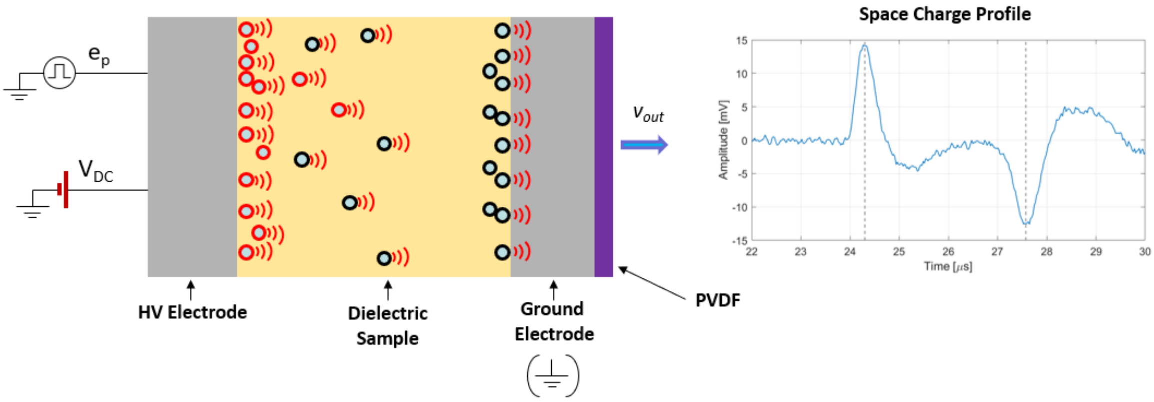

Figure 2.3: PEA setup diagram for flat sample.

coupled to the piezoelectric transducer is used, but this solution is limited to a single diameter and is sensitive to the quality of the acoustic contact. To overcome these limitations, setup with flat electrodes and polymeric acoustic couplers (e.g. PMMA or polystyrene) have been developed, which improve the acoustic impedance matching with the cable insulation and ensure greater sensitivity of the PVDF transducer [27, 28]. The high voltage pulse is applied directly to the outer semiconductive layer of the cable, so that it passes radially through the insulation to the central conductor, while the measuring equipment remains at earth potential. In this way, the impulsive electric field interacts with the trapped charges, generating the acoustic wave, which passes through the polymeric coupler and is detected by the transducer. This configuration not only simplifies the experimental connection, but also allows reliable measurements to be performed even on full-scale cables, maintaining high sensitivity and reducing the effects of noise and unwanted reflections. Although this method is easy to apply to mini cables, full-size cables require the removal of the outer sheath and metal shield in order to connect the sensor and metal rings for pulse application. A diagram showing how to apply the PEA method for full-size cables is shown in Fig. 2.4. This configuration makes the PEA technique a destructive measurement method for full-size cables. However, this technique allows for real-time profiling of the charge distribution, providing invaluable insights into the space charge dynamics under various operating conditions.

2.3 PEA Signal Post Processing

The raw signal acquired by the oscilloscope is recorded as a voltage waveform over time, which is indirectly related to the radial distribution of charge within the insulator. However, it does not provide a direct representation of the actual space charge distribution. The measured signal is affected by several distortion factors, including the frequency response of

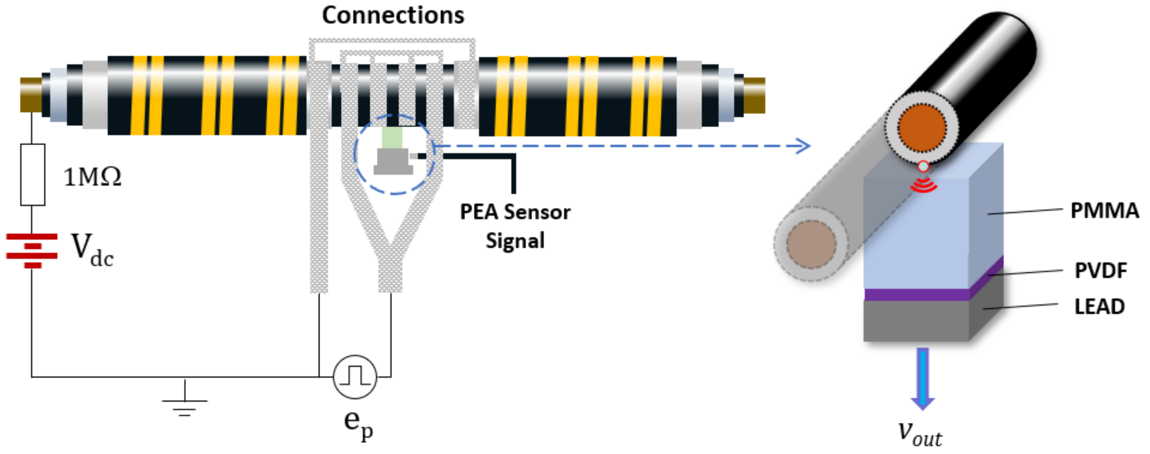

Figure 2.4: PEA setup diagram for full-size cables.

the measurement system, the cylindrical geometry of the cable, and the acoustic attenuation and dispersion characteristics of the dielectric material. Consequently, reconstructing the true space charge profile, and subsequently deriving the corresponding electric field, requires a rigorous, multi-step signal processing procedure [29, 30]. Any error or oversimplification in this stage may result in a misleading interpretation of the underlying physical phenomena occurring within the cable. The complete processing pipeline, as established in the literature and applied in this work, can be divided into five main steps:

Preconditioning: In some cases, the acquired signal requires pre-processing before it can be reliably analyzed. Due to limitations of the measurement setup, the recorded profile can shows an offset, which can be corrected either during acquisition, by adjusting the oscilloscope settings, or in post-processing, by subtracting the mean value. A further issue arises when the piezoelectric sensor thickness is not properly matched to the excitation pulse width. In this condition, the PEA signal may shift toward the trailing edge of the pulse, producing a monotonically increasing or decreasing baseline (Fig. 2.5). Such distortions can be corrected via software by restoring a flat baseline, either through subtraction of the best-fit linear trend or, alternatively, by removing a signal acquired without applied DC voltage [31, 32]. At the end, the oscilloscope can be configured to enhance the Signal-to-Noise Ratio (SNR) by averaging multiple acquisitions. The number of profiles to be averaged depends on the noise level during the experiment and can range from a few thousand to several tens of thousands [24].

Deconvolution: The measured signal $y(t)$ can be mathematically described as the convolution

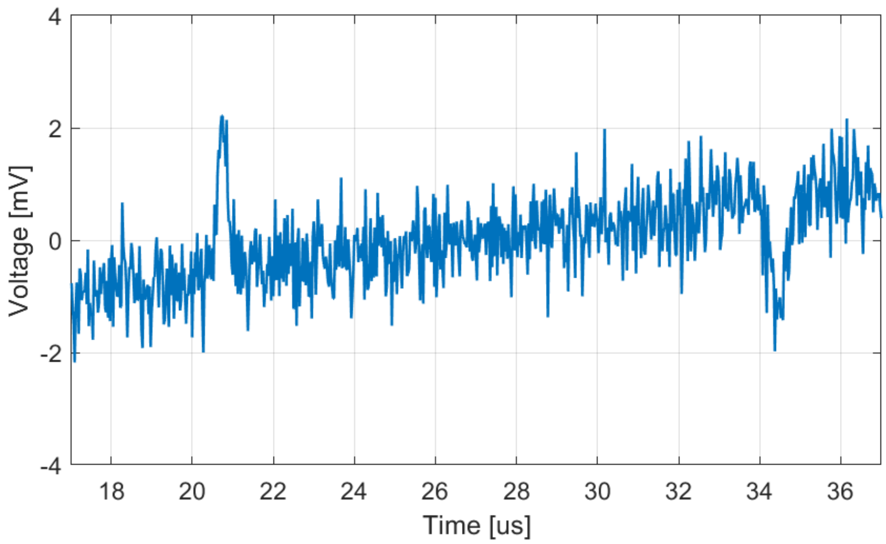

Figure 2.5: Example of a PEA profile in the presence of baseline distortion.

of the original acoustic signal at the sensor's input, $x(t)$, with the impulse response of the measurement system, $h(t)$, plus additive noise $n(t)$ [31]:

$$y(t) = x(t) * h(t) + n(t) \tag{2.3}$$

The function $h(t)$ represents the response of the entire detection system, including the PEA cell, piezoelectric transducer, and amplifier. To accurately reconstruct the true acoustic signal, $x(t)$, an inverse operation, called deconvolution, must be performed. This step is fundamental for correcting the distortions introduced by the sensor and ensuring the fidelity of the final space charge profile. The choice of the deconvolution technique significantly influences the quality of the reconstructed signal, with inherent trade-offs between computational efficiency, noise suppression, and signal accuracy. As this is a crucial step, several techniques are described in details in the following section.

Geometric Correction: In a flat specimen, the electric field generated by the high voltage pulse (e_p) is uniform across the thickness (d) and equal to e_p/d. As a result, any charge present, whether at an interface or within the dielectric bulk, experiences the same impulsive force regardless of its position. In a coaxial cable, however, the situation differs. The Laplacian electric field E_p produced by the pulse is not constant but changes with the radius (r), reaching its maximum near the inner conductor and decreasing towards the outer semiconductive layer, as expressed by:

$$E_p(r) = \frac{e_p}{r \cdot \ln\left(\frac{R_{outer}}{R_{inner}}\right)} \tag{2.4}$$

This implies that an identical amount of charge generates a stronger acoustic wave when located near the inner semiconductive layer, where the field is higher, and a weaker wave when near the outer layer, where the field is lower. To eliminate this positional dependency and ensure that the deconvolved signal reflects only the charge density, the signal must be normalized. Using the field at the outer radius as a reference, the entire profile is divided by a correction factor K_1, defined as the ratio between the field at radius r and that at R_{outer} [29, 33, 34]:

$$K_1 = \frac{E(r)}{E(R_{outer})} = \frac{R_{outer}}{r} \tag{2.5}$$

Applying this correction factor effectively equalizes the stress across the insulation, making the resulting profile equivalent to that of a flat specimen where the stress is uniform. However, this is not the only aspect related to cylindrical geometry to consider. The second geometric effect is the intrinsic attenuation of the acoustic wave during radial propagation. A pressure wave generated at the inner interface distributes its energy over an expanding cylindrical surface as it travels toward the outer interface. Consequently, its amplitude decreases with distance, following a $1/\sqrt{r}$ dependence [29, 33]. This phenomenon, known as geometric divergence, means that the wave detected by the sensor from the inner interface is weaker than the wave that was originally generated. To compensate for this attenuation, the signal is amplified by a factor that counteracts the radial decay. The correction factor K_2 is defined as the ratio between the amplitude of the acoustic wave at a generic position r and its amplitude at the detection point [29, 33, 34]:

$$K_2 = \sqrt{\frac{r}{R_{outer}}} \tag{2.6}$$

It is essential to note that both geometric correction factors are a function of the radial position and are normalized to unity at the outer radius, which serves as the reference point for the entire process. This choice is physically based on the nature of the measurement in a cylindrical geometry. The primary effect of the geometric distortion is experienced by the pressure wave originating from the inner interface. This wave is generated by a stronger impulsive electric field, as the field in a coaxial cable is inversely proportional to the radius ($E(r) \propto 1/r$), but it subsequently attenuates during its propagation towards the sensor due to geometric divergence. Conversely, the pressure wave originating at the outer interface can be considered unaffected by these intrinsic distortions before reaching the PEA cell. It is generated by the weakest electric field within the dielectric and, given its proximity to the sensor, undergoes negligible propagation related attenuation. The purpose of the geometric correction, therefore, is to mathematically transform the internally generated wave to the same reference conditions as the external wave, compensating for both the greater generation force and the subsequent propagation attenuation. Fig. 2.6 shows an example of geometric correction for a simulated PEA profile for a cable with insulation having an inner radius of 32 mm and an outer radius of 52 mm.

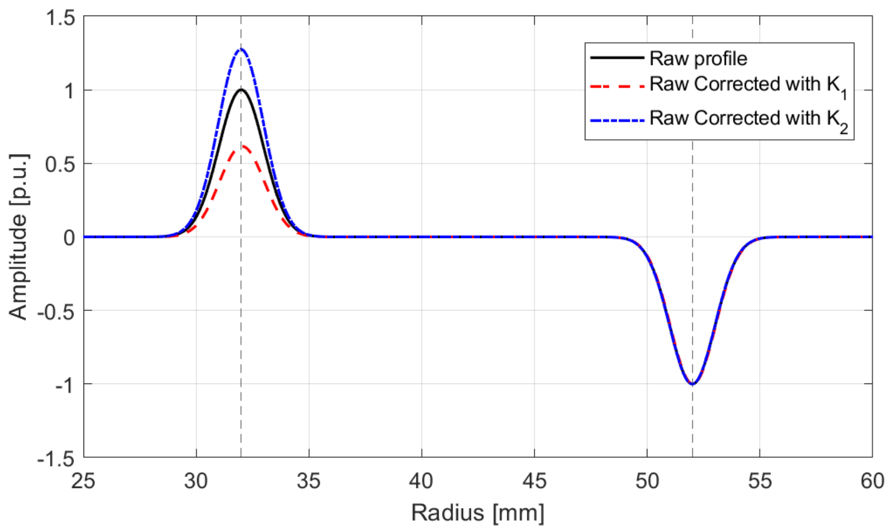

Figure 2.6: Simulated PEA profile with geometric corrections.

Attenuation and Dispersion Correction: Acoustic waves propagating in a cylindrical medium are subject not only to geometric divergence, which attenuates the amplitude, but also to additional attenuation arising from the dissipative nature of the material. In particular, the polymeric insulator is not an ideal propagation medium, and part of the wave energy is absorbed, leading to further amplitude decay. This attenuation is frequency dependent, as higher frequency components are damped more rapidly than lower frequency ones. Moreover, the propagation speed of the acoustic wave also changes with frequency, leading to dispersion that manifests as a phase shift among the different frequency components of the wave spectrum. The combined effect of attenuation and dispersion results in a broadening of the acoustic wave generated at the inner insulation interface. To quantify and correct these effects, the acoustic wave can be modeled using the solution of the wave equation in cylindrical coordinates for a viscoelastic medium [34, 35]. Under these assumptions, the wave $p(r,t)$ can be written as

$$p(r,t) = p_0\, e^{j[k(j\omega)r - \omega t]}, \tag{2.7}$$

where the complex wave number $k(j\omega)$ is defined as

$$k(j\omega) = \beta(\omega) + j\alpha(\omega). \tag{2.8}$$

Here, $\alpha(\omega)$ represents the attenuation constant, describing the exponential decay of the wave amplitude during propagation, while $\beta(\omega)$ is the phase constant, governing the phase evolution of the wave and accounting for dispersion effects. For correction purposes, expression 2.7 is transformed into the frequency domain using Fourier analysis. Denoting the frequency spectrum of the wave at a distance d as $P(\omega, d)$ and the spectrum at the origin as $P(\omega, 0)$, the transfer function $G(\omega, d)$ is defined as the ratio of these spectra:

$$G(\omega, d) = \frac{P(\omega, d)}{P(\omega, 0)} = e^{-[\alpha(\omega)+j\beta(\omega)]\cdot d} \tag{2.9}$$

From this relation, the attenuation and phase constants can be estimated by analyzing the magnitude and phase of $G(\omega, d)$. Specifically, for a propagation distance equal to the medium thickness d, they are given by [36, 37]:

$$\alpha(\omega) = -\frac{1}{d} \ln|G(\omega, d)| \tag{2.10}$$

$$\beta(\omega) = -\frac{1}{d} \angle G(\omega, d) \tag{2.11}$$

By estimating $\alpha(\omega)$ and $\beta(\omega)$, for example, by comparing the propagated internal wave to the external reference wave which does not undergo such degradation, the propagation transfer function $G(\omega, r)$ can be fully determined. This function provides a complete mathematical model of the attenuation and dispersion effects in the frequency domain. The correction is then performed by applying an inverse filter based on this transfer function to the measured signal. This process effectively restores the amplitude and sharpness that the internal wave possessed at the moment of its generation, thus allowing for an accurate estimate of the space charge density. Fig. 2.7 shows an example of the results obtained by implementing this correction process.

Calibration: Even once distortions from the measurement cell, cable geometry, and propagation medium have been corrected, the signal fundamentally retains its nature as a voltage measurement. The final step in the processing pipeline is the conversion of the processed voltage profile into a physically meaningful space charge distribution expressed in

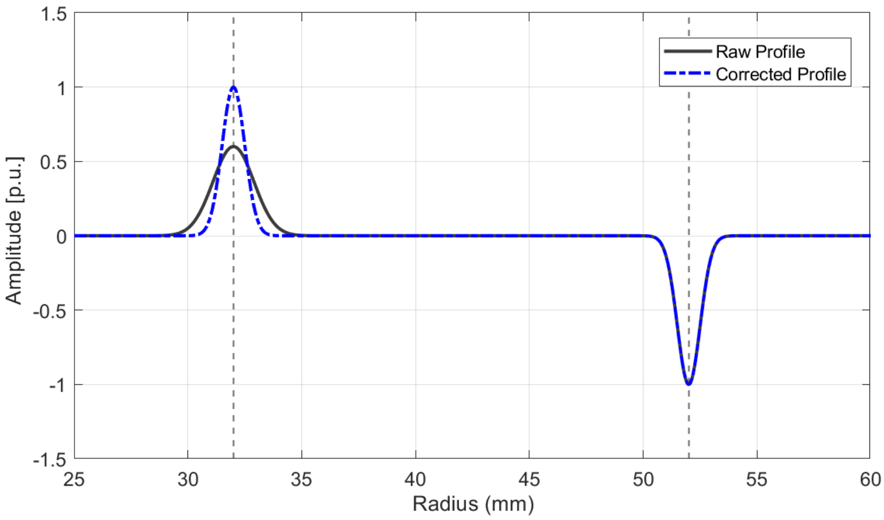

Figure 2.7: Simulated PEA profile with attenuation and dispersion corrections.

C/m^3. The calibration process is performed by comparing a feature of the processed signal with a known theoretical value. Since the space charge distribution is initially unknown, the procedure relies on the surface charge induced at the dielectric/semicon interface by the applied DC voltage. Specifically, the outer peak of the PEA signal obtained at this stage of the process is used again as the reference. This choice is motivated by the fact that the outer peak originates from the interface directly adjacent to the sensor and therefore undergoes the least amount of distortion from acoustic propagation effects, making it the most reliable feature in the signal. The procedure can only be performed on a reference profile acquired in the absence of significant accumulated space charge, ensuring that the measured surface charge corresponds accurately to the theoretically expected value, without any injection phenomenon. The expected surface charge density, q_0, at the outer interface, r_{outer}, is calculated based on the cable's geometry and the applied voltage, V_{DC}, using the following relationship derived from electrostatics for coaxial capacitor [32, 38]:

$$q_0 = \epsilon_r \epsilon_0 \frac{V_{DC}}{r_{outer} \cdot ln(\frac{r_{outer}}{r_{inner}})} \tag{2.12}$$

where ϵ_r and ϵ_0 are the relative and vacuum permittivity respectively. A calibration factor is then introduced as a proportionality coefficient between the known theoretical charge and the area of outer peak (Fig. 2.8)[39]. In practice, it is obtained as the ratio between the integral of the outer peak of the corrected profile, $\bar{x}(r)$, and the surface charge density:

$$K_{cal} = \frac{\int_{r1}^{r_2} \bar{x}(r)dr}{q_0} \tag{2.13}$$

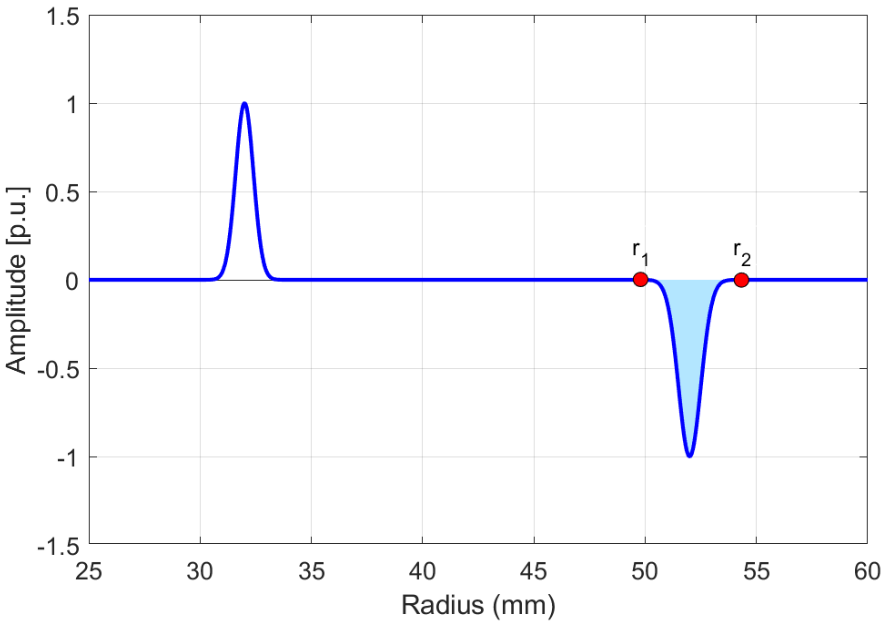

Figure 2.8: Corrected profile ready for the calibration process. The outer peak area is related to the expected surface charge density, based on the applied voltage, to determine the calibration coefficient. The radii r_1 and r_2 are the integration limits.

This factor, which includes the overall sensitivity of the measurement system, is subsequently applied to the entire signal. The entire voltage waveform is scaled correctly, converting it into an charge density profile, $\rho(r)$, as a function of the radial position.

$$\rho(r) = \frac{\bar{x}(r)}{K_{cal}} \tag{2.14}$$

This calibrated profile forms the basis for all subsequent analysis, including the calculation of the electric field distribution.

Electric Field Calculation: Once the space charge distribution, $\rho(r)$, has been determined, it is possible to calculate the radial electric field profile through the thickness of the insulator. The evaluation is derived from Gauss's law in differential form expressed in cylindrical coordinates. The relationship between charge density and electric field is given by the following equation [33, 38]:

$$\frac{dE(r)}{dr} + \frac{1}{r}E(r) = \frac{\rho(r)}{\epsilon_0\ \epsilon_r} \tag{2.15}$$

the general solution of 2.15 is:

$$E(r) = \frac{1}{r\ \epsilon_0\ \epsilon_r}\int_{r_{inner}}^{r_{outer}} r\ \rho(r)\ dr + \frac{C}{r} \tag{2.16}$$

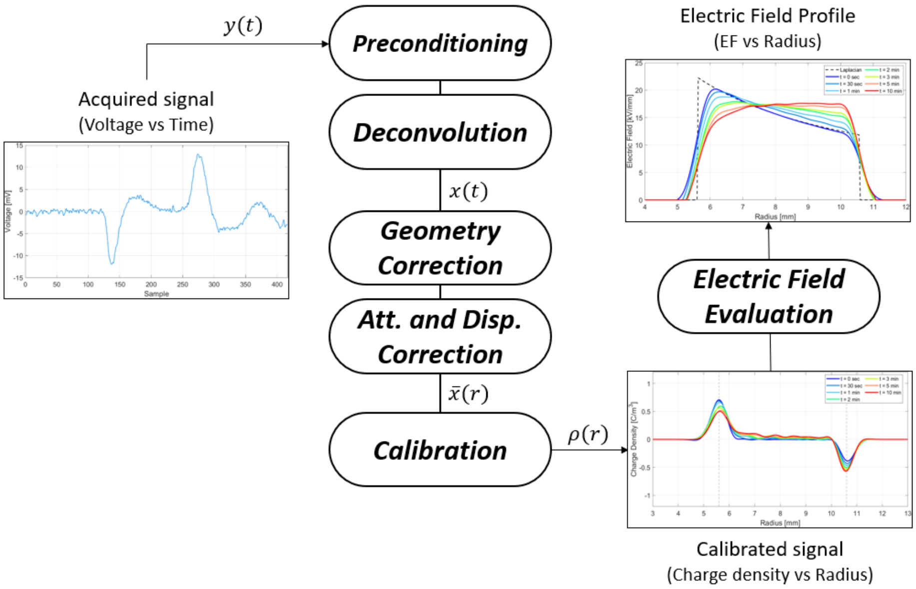

Figure 2.9: Steps in processing the raw signal to obtain the charge distribution and the corresponding electric field profile.

where r_{inner} and r_{outer} are the inner and outer radius respectively, and C is a constant [39, 40, 41, 42]. The latter is chosen consistently with the boundary condition requiring that the integral of the electric field across the dielectric thickness equals the applied voltage.

$$\int_{r_{inner}}^{r_{outer}} E(r)\, dr = V_{DC} \tag{2.17}$$

This constraint ensures that the solution is physically consistent. The result of this process is a detailed profile of the electric field that includes both the geometric component (Laplacian) and the distortion contribution generated by the space charge. This profile serves as a fundamental diagnostic indicator of the electrical stress within the insulator.

The entire process pipeline is reported in Fig. 2.9. Among these steps, deconvolution represents the most challenging and decisive operation, as its implementation strongly influences the accuracy, resolution, and robustness of the reconstructed profile. Given its complexity and relevance within the post-processing framework, a dedicated section is provided to describe the adopted methodology and to present the results of its application.

2.4 The Role of Deconvolution

As mentioned in the previous section, the aim of the deconvolution process is to find an accurate estimate of the original acoustic signal, $x(t)$, from the acquired signal, $y(t)$, by solving the inverse problem for the equation. 2.3. The selection of an appropriate deconvolution method is an important decision in the PEA signal processing pipeline, representing the trade-off between computational efficiency, noise suppression, and the fidelity of the reconstructed signal [43]. As demonstrated in the literature, deconvolution approaches have distinct advantages and are tailored to specific types of signals and experimental conditions. Each technique exhibits particular strengths depending on factors such as noise level, signal resolution, and presence of distortions. In general, these methods can be classified according to the domain in which they operate: frequency domain techniques, which exploit the spectral characteristics of the signal to perform filtering and inversion, time domain techniques, which directly manipulate the signal waveform to correct distortions, and hybrid approaches, which combine aspects of both domains to achieve a balance between accuracy and computational efficiency. The choice of the most suitable method therefore depends on the properties of the acquired signal and the objectives of the analysis.

2.4.1 Frequency Domain Deconvolution

These methods rely on the convolution theorem [44], which states that a convolution in the time domain corresponds to a simple multiplication in the frequency domain. By transforming the acquired signal and the system response into the frequency domain, the deconvolution problem is reduced to an algebraic division, where the spectrum of the original signal is obtained by dividing the spectrum of the measured signal by that of the system response. This approach not only simplifies the mathematical treatment but also significantly reduces the computational complexity, particularly for long signals, as the Fast Fourier Transform (FFT) algorithm can be efficiently employed to perform the forward and inverse transformations. Moreover, working in the frequency domain allows for straightforward implementation of filtering strategies to suppress noise, compensate for system bandwidth limitations, and mitigate the amplification of high-frequency components, which are common challenges in practical deconvolution applications. The main techniques found in the literature are listed below.

Fourier Deconvolution: This is the most direct implementation of the inverse filtering

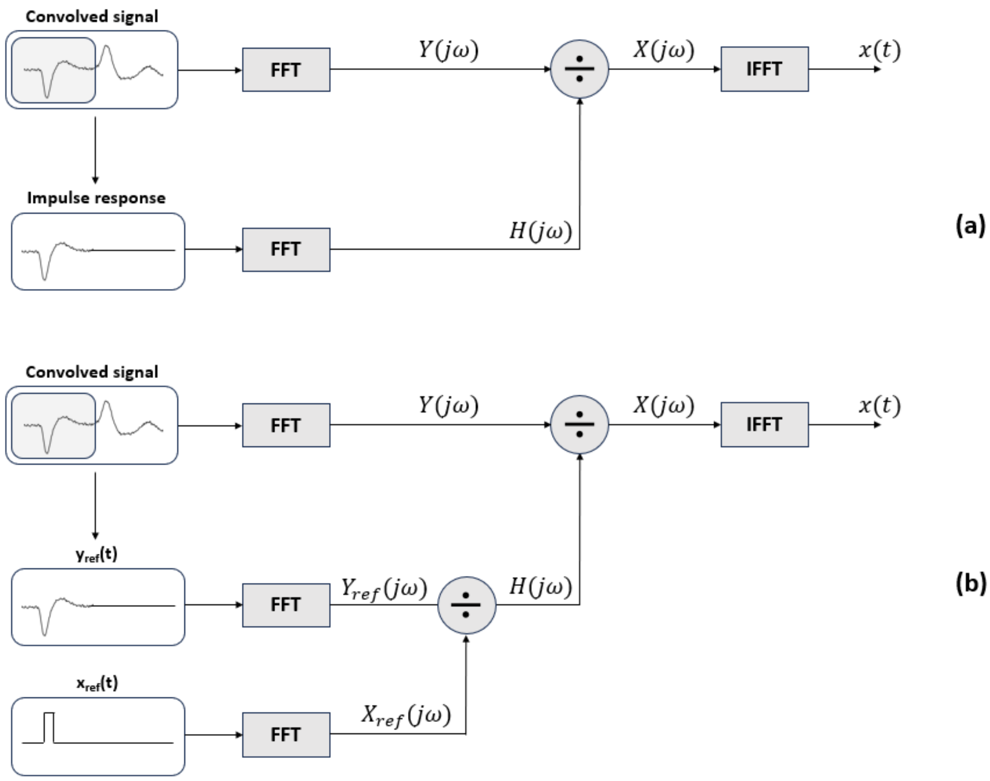

Figure 2.10: Block diagrams of two different Fourier deconvolution methods. (a) The outer peak of the profile $x(t)$ is approximated to the impulse response of the PEA cell. (b) The impulse response is estimated by first deconvolving the outer peak with a reference signal that has the characteristics of the applied impulse.

process. According to the convolution theorem, the spectrum of the deconvolved signal, $X(j\omega)$, is obtained by dividing the spectrum of the measured signal, $Y(j\omega)$, by the system transfer function, $H(j\omega)$ [45, 38]:

$$X(j\omega) = \frac{Y(j\omega)}{H(j\omega)} \tag{2.18}$$

The transfer function $H(j\omega)$ is typically estimated either by using the outer peak of the raw PEA signal as an approximation of the system's impulse response or through a two-step deconvolution process with a known reference pulse (e.g., a square or triangular wave) [46]. This procedure is motivated by the fact that the raw signal always contains the response of the measurement system, which acts as a band limited filter on the true acoustic wave. Since the exact impulse response of the setup is generally not available, practical approximations must be employed. The direct use of the outer peak relies on the fact that it is primarily governed by the excitation impulse, which is commonly approximated as Dirac-like, and thus provides a good representation of the instrumental response. In contrast, reference based methods offer a more controlled strategy to characterize the system under well defined excitation conditions.

In both cases, the objective is to derive a reliable estimate of $H(j\omega)$ that enables compensation for the distortion introduced by the measurement cell. Although simple and fast, this method is highly susceptible to noise. The division by near-zero values in the spectrum of $H(j\omega)$ can drastically amplify high frequency noise, leading to an unstable result with a low Signal-to-Noise Ratio (SNR) and significant baseline distortions. This necessitates the use of a low pass filter, which introduces its own trade-offs between noise reduction and the loss of important signal details. Fig 2.10 shows two block diagrams summarizing the two main deconvolution techniques using the Fourier transform.

Wiener Deconvolution: The Wiener filter can be used as an enhancement of the Fourier method that provides simultaneous noise suppression and signal recovery. It operates by incorporating statistical information about the original signal and the noise into the deconvolution process [47, 48]:

$$X(j\omega) = Y(j\omega)\ W(j\omega) = Y(j\omega)\ \frac{H^*(j\omega)}{|H(j\omega)|^2 + SNR} \tag{2.19}$$

The transfer function, $W(j\omega)$, is designed to minimize the mean square error between the estimated and the true signal. In practice, since the exact power spectra of the signal and noise are rarely known, the filter is often implemented with a regularization parameter, γ_W, which approximates the SNR and stabilizes the inversion process:

$$X(j\omega) = Y(j\omega)\ \frac{H^*(j\omega)}{|H(j\omega)|^2 + \gamma_W} \tag{2.20}$$

Although it performs better than simple inverse filtering in the presence of noise, it often suffers from the same baseline distortion issues as the standard Fourier method and its effectiveness depends on the proper tuning of the regularization parameter [49]. Fig. 2.11 shows a block diagram for implementing the deconvolution technique using a Wiener filter.

Iterative Blind Deconvolution (IBD): Beyond the direct filtering approaches, more advanced iterative methods operating in the frequency domain have also been developed, such as IBD. This technique is particularly useful when the system's transfer function, $H(j\omega)$, is not accurately known. IBD is a "blind" algorithm that simultaneously estimates both the original signal, $x(t)$, and the system's impulse response, $h(t)$, from the measured output, $y(t)$. The process begins with initial estimate for the signal and the system response and

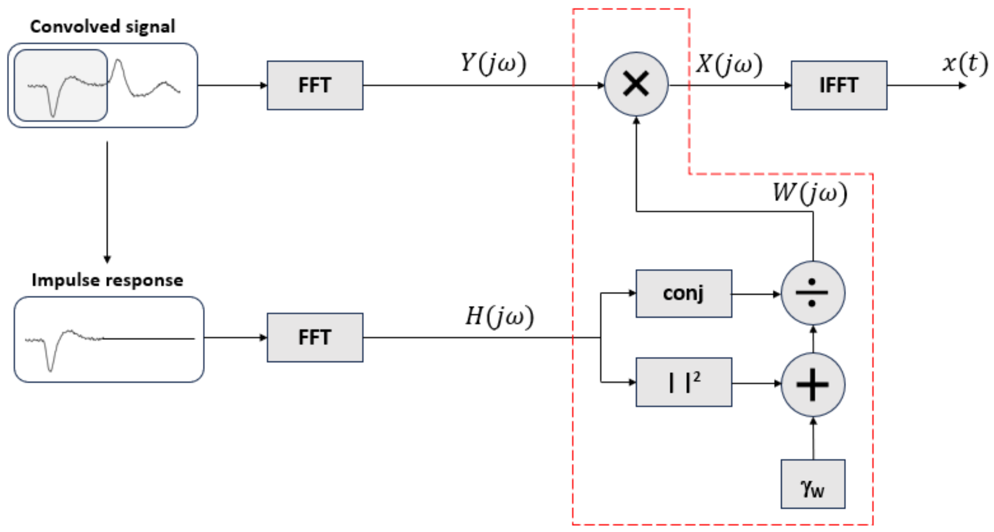

Figure 2.11: Block diagram of deconvolution using a Wiener filter.

then iteratively refines these estimates by applying a Wiener-like filter in each step until a convergence criterion is met:

$$H_k(j\omega) = \frac{Y(j\omega)X^*_{k-1}(j\omega)}{|X_{k-1}(j\omega)|^2 + \frac{\alpha}{|H_{k-1}(j\omega)|^2}} \tag{2.21}$$

$$X_k(j\omega) = \frac{Y(j\omega)H^*_k(j\omega)}{|H_k(j\omega)|^2 + \frac{\alpha}{|X_{k-1}(j\omega)|^2}} \tag{2.22}$$

where k is the iteration index and α is the noise related parameter. While this method offers the significant advantage of not requiring prior knowledge of the system's characteristics, its main drawback is that the solution is not unique and its accuracy is highly dependent on the initial assumptions and constraints imposed on the algorithm. Fig. 2.12 shows a block diagram for implementing the deconvolution using a IBD technique.

2.4.2 Time Domain Deconvolution

Time domain deconvolution techniques formulate the deconvolution problem as a system of linear equations directly in the time domain. Considering Eq. 2.3 in discrete form, the acquired signal can be expressed using matrix notation as:

$$\mathbf{y} = \mathbf{H} * \mathbf{x} + \mathbf{n}, \tag{2.23}$$

where $\mathbf{y}$ is the vector of measured signal samples, $\mathbf{x}$ represents the unknown original signal, $\mathbf{n}$ accounts for additive noise, and $\mathbf{H}$ is a Toeplitz matrix constructed from the system's impulse

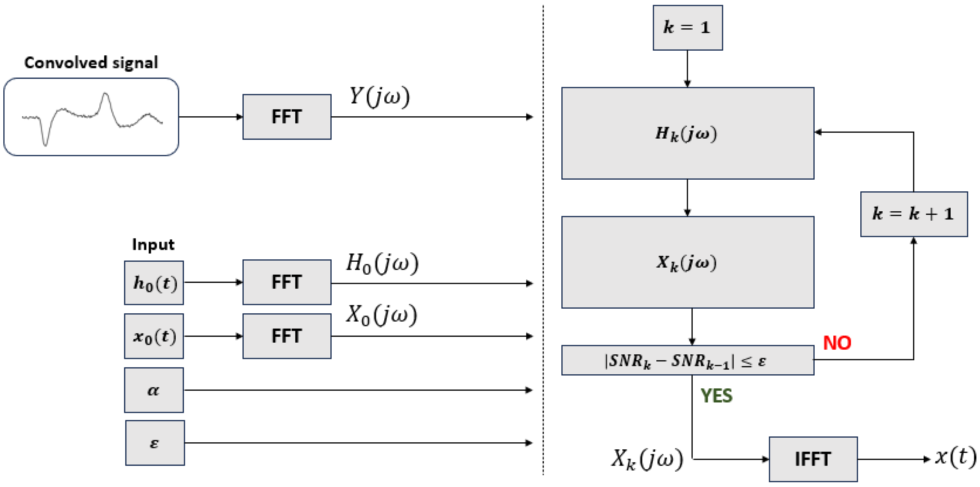

Figure 2.12: Block diagram of deconvolution using IBD technique.

response. The Toeplitz structure arises because each row of the matrix corresponds to a time shifted version of the impulse response, reflecting the convolution operation in discrete [50]. Direct inversion of $\mathbf{H}$ to solve for $\mathbf{x}$ is generally not feasible, as the system is typically ill-conditioned, meaning that small perturbations in the measured signal (due to noise) can lead to large errors in the reconstructed signal [51]. To address this challenge, specialized solution methods are employed, such as regression based approaches and regularization techniques. These methods introduce additional constraints or penalty terms that stabilize the inversion process, suppress the amplification of noise, and improve the robustness of the solution [52]. Time domain deconvolution has the advantage of providing fine temporal resolution and flexibility in handling non-stationary signals, making it particularly suitable for signals with sharp features or when the system response exhibits significant temporal variations. However, it is computationally more intensive than frequency domain methods, especially for long signals, and requires careful tuning of the regularization parameters to balance accuracy and noise suppression.The main techniques found in the literature are listed below.

Direct Time Domain Deconvolution: This method finds an estimate of the signal $\mathbf{x}$ by minimizing a cost function using the Least Squares Error (LSE) method [53]. The cost function $J(\mathbf{x})$ is equal to the 2-norm of the estimation error plus a second term:

$$J(\mathbf{x}) = ||\mathbf{y} - \mathbf{H}\mathbf{x}||_2^2 \; + \; \lambda_{TD}||\mathbf{x}||_2^2 \qquad (2.24)$$

To overcome the ill-conditioned nature of the problem, the Tikhonov regularization term, $\lambda_{TD}||\mathbf{x}||_2^2$, is added to the cost function, where λ_{TD} is a regularization parameter. The

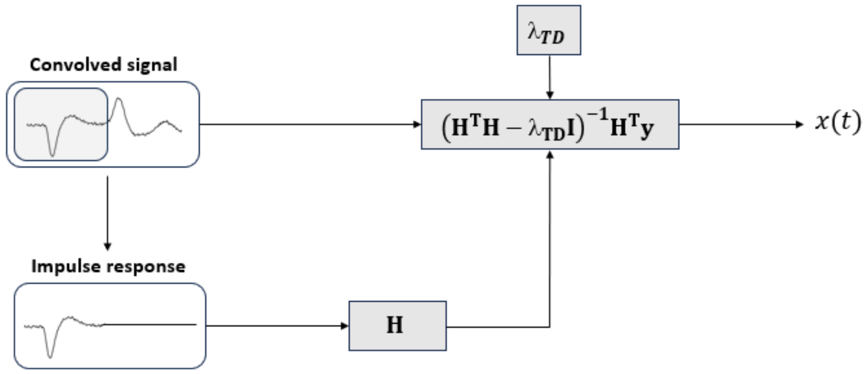

Figure 2.13: Block diagram of time domain deconvolution.

closed-form solution of 2.24 is:

$$\mathbf{x} = (\mathbf{H}^T\mathbf{H} + \lambda_{TD}\mathbf{I})^{-1}\mathbf{H}^T\mathbf{y} \tag{2.25}$$

where $\mathbf{I}$ is the identity matrix. This approach is highly effective at preserving low frequency components, resulting in a stable baseline free from the distortions common in frequency domain methods. However, it is computationally very expensive because of the large matrix inversion involved and requires a careful tuning of the regularization parameter, often performed using other techniques like the L-curve analysis [54]. Fig. 2.13 shows a block diagram for implementing the time domain deconvolution.

Sparse Deconvolution: This technique is based on the assumption that the desired signal $x(t)$ is sparse, meaning that it consists of only a few significant localized components (e.g. peaks at the interfaces) [55, 56]. From a mathematical point of view, the problem is analogous to the previous one, with the only difference being that, due to the sparsity constraint, the cost function adjustment term is modified:

$$J(\mathbf{x}) = ||\mathbf{y} - \mathbf{H}\mathbf{x}||_2^2 \; + \; \lambda_{SD}||\mathbf{x}||_1 \tag{2.26}$$

In this case, a term related to 1-norm of $\mathbf{x}$ is used. Since this cost function is not differentiable everywhere, the solution must be found using an iterative algorithm, such as the Majorization-Minimization (MM) method [57]. A diagram illustrating the application of this algorithm is shown in Fig. 2.14. This technique can achieve excellent resolution and is highly effective in noise suppression, making it ideal for detecting localized charge accumulations, such as in measurements with flat, multi-layer samples. Its main drawbacks are its high computational

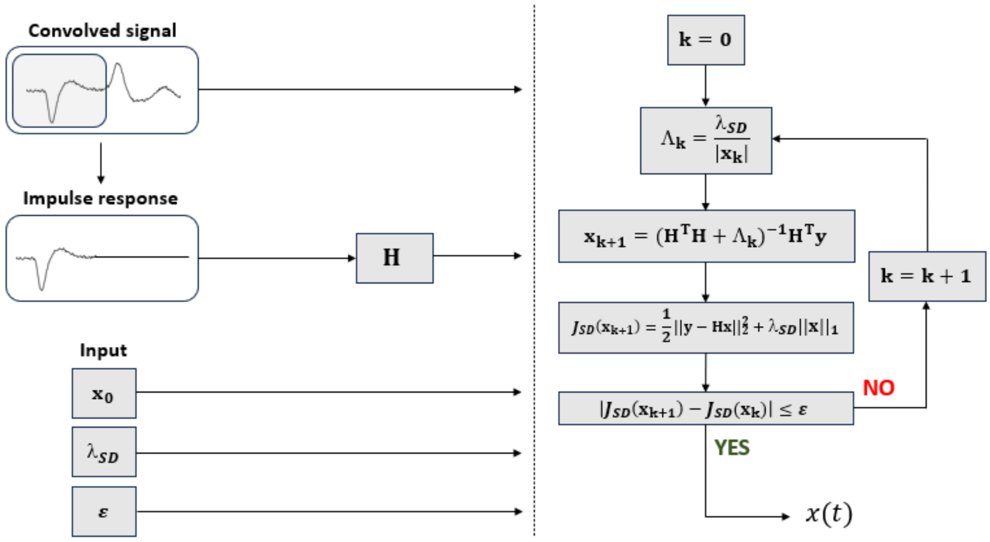

Figure 2.14: Block diagram of sparse deconvolution.

cost and the dependence on the regularization parameter, λ_{SD}, along with the fact that the sparsity assumption may not be valid for all types of space charge distributions.

2.4.3 Hybrid Domain Deconvolution

These methods aim to combine the strengths of both time and frequency domain approaches in order to achieve a balance between computational efficiency and reconstruction accuracy. By exploiting spectral information, they can effectively suppress noise and handle bandwidth limitations, while the direct time domain treatment allows for finer control over waveform features and compensation of local distortions. Hybrid strategies are therefore particularly useful in situations where neither domain alone provides satisfactory results, such as when signals are affected simultaneously by broadband noise and time localized artefacts. In this way, they provide a flexible framework that adapts to the specific characteristics of the acquired signal and the requirements of the analysis. The main techniques found in the literature are listed below.

Dual Domain Deconvolution: This technique reconstructs the final signal by merging two separate components. The stable, low frequency content (which defines the baseline) is obtained from a computationally cheaper, downsampled time domain deconvolution. The high frequency details are obtained from a standard frequency domain deconvolution. This approach effectively reduces baseline distortions while preserving high resolution. However, its success is critically dependent on the criteria used to merge the two spectral parts, and the

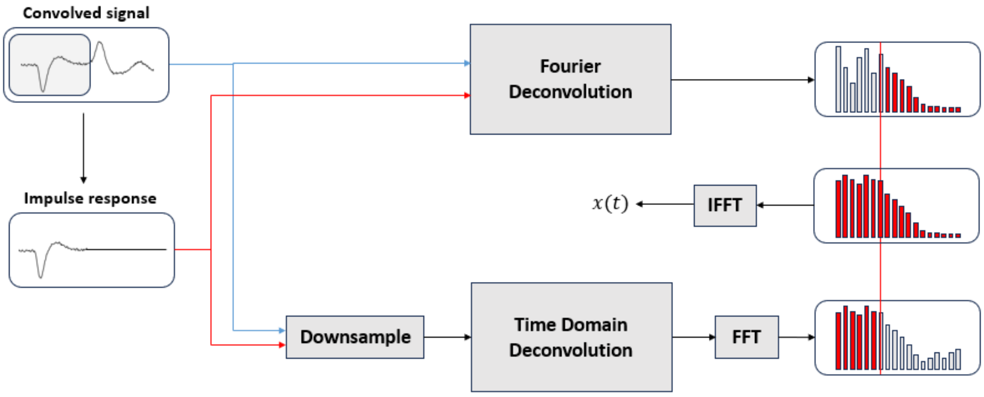

Figure 2.15: Block diagram of dual domain deconvolution.

downsampling process can risk a loss of signal detail if not calibrated correctly. Fig. 2.15 shows a block diagram for implementing the dual domain deconvolution.

Short Time Fourier Transform (STFT) Based Deconvolution: This technique extends the principles of Fourier deconvolution into the time frequency domain by using the STFT. Instead of providing a single, global representation of a signal's frequency content, the STFT divides the signal into short, overlapping time segments and applies a Fourier transform to each. This process generates a spectrogram, which reveals how the frequency content of the signal evolves over time. The deconvolution is then performed as a localized division in this time frequency domain. This approach is particularly well suited for non-stationary signals and can effectively reduce baseline distortions while preserving temporal information. However, its performance is critically dependent on the choice of the window function and its width, which introduces a fundamental trade-off between time and frequency resolution. In [58] this technique is implemented through a two step deconvolution process. In the first step, the transfer function of the acquisition system, $H(t, f)$, is determined by calculating the ratio between the transform of an acquired profile at reduced voltage, $Y_{ref}(t, f)$, and a reference signal representing the ideal profile of the applied pulse, $X_{ref}(t, f)$:

$$H(t, f) = \frac{Y_{ref}(t, f)}{X_{ref}(t, f)} \tag{2.27}$$

Once $H(t, f)$ has been determined, the acquired profile at the desired voltage is then deconvoluted:

$$X(t, f) = \frac{Y(t, f)}{H(t, f)} \tag{2.28}$$

Fig. 2.16 shows a block diagram for implementing the STFT based deconvolution.

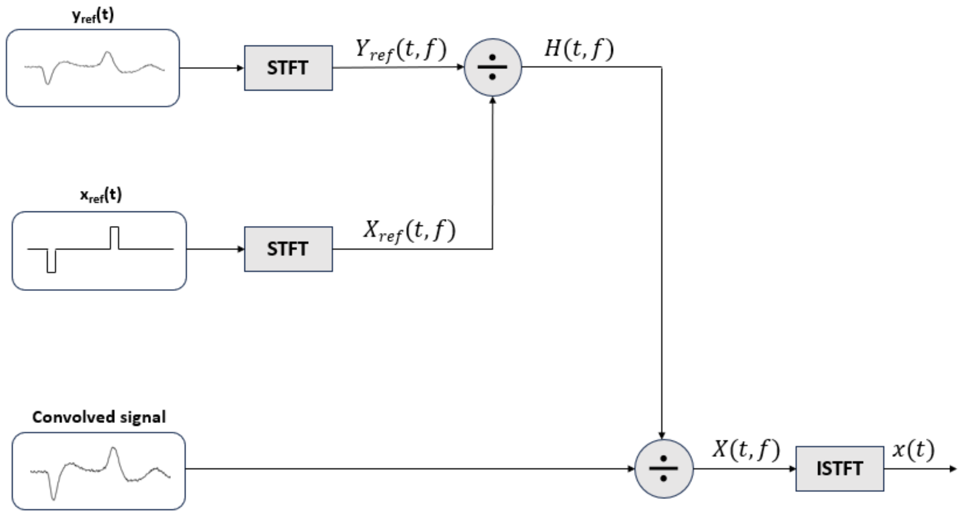

Figure 2.16: Block diagram of STFT based deconvolution.

Laplace Deconvolution: This method is specifically designed to address a common failure point of Fourier deconvolution: the distortion caused by long decaying signal tails. Such tails, which may result from multiple reflections or non-optimal acoustic coupling, often introduce low frequency components that corrupt the signal's baseline [59]. Laplace deconvolution mitigates this by applying an exponential weighting factor (τ) to the signal before performing the Fourier transform. This weighting effectively suppresses the influence of the signal's tail. The Laplace transform $\mathcal{L}\{\cdot\}$ of the time function $x(t)$ is defined by the following equation:

$$\mathcal{L}\{x(t)\} = \int_{-\infty}^{\infty} x(t)\ e^{-(\frac{1}{\tau}+j\omega)t}\ dt \tag{2.29}$$

By decomposing the exponential term and introducing the following quantity:

$$\bar{x}(t) = x(t)\ e^{\frac{t}{\tau}} \tag{2.30}$$

the Fourier transform of the signal $\bar{x}(t)$ coincides with the Laplace transform of $x(t)$ for a fixed value of τ. Therefore, considering τ as a parameter rather than a variable, we obtain a simple implementation of Laplace deconvolution through FFT algorithms. In this case, τ becomes an adjustment parameter. After the standard deconvolution is performed in the frequency domain, the result is transformed back to the time domain, and the initial weighting is removed by applying an inverse exponential factor ($e^{-t/\tau}$). While this technique is highly effective at improving baseline stability, its success requires the careful tuning of the time constant parameter [60]. Fig. 2.17 shows a block diagram for implementing the Laplace

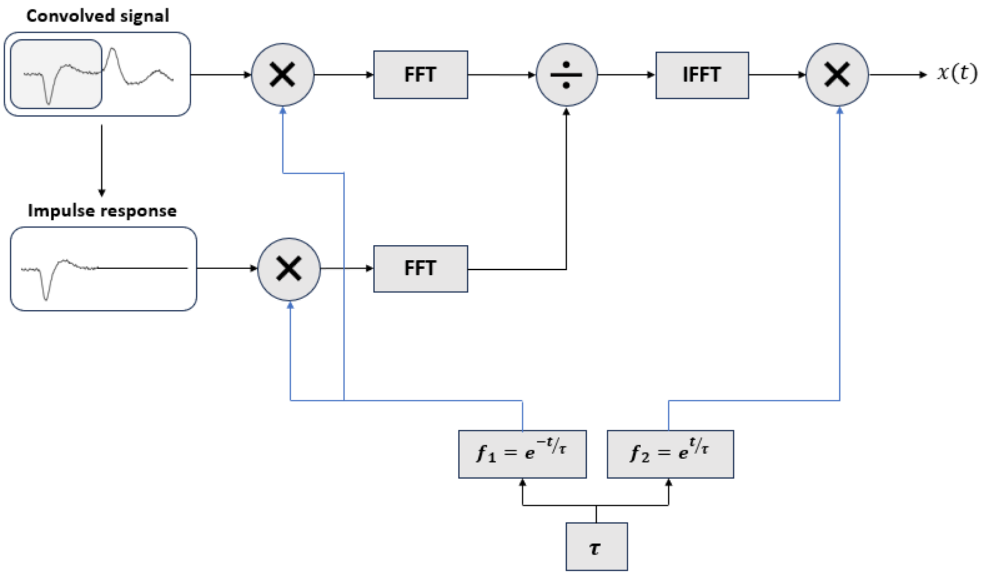

Figure 2.17: Block diagram of Laplace deconvolution.

deconvolution.

2.5 Experimental PEA Setup for HVDC Cables

The experimental investigations presented in this thesis have been conducted using a dedicated measurement system designed for PEA signal acquisition. The setup has been tested on various Device Under Test (DUT) scales, from laboratory models to industrial components. This comprehensive approach allowed for both the development and the validation of the entire measurement chain under realistic conditions. A key element of the hardware is the PEA measurement cell, which has been designed and constructed by the research team of Professor Pietro Romano, Head of L.E.PR.E. HV Laboratory of the University of Palermo [61, 62]. The cell's design incorporates the latest scientific optimizations, such as a plexiglass acoustic coupler, to ensure high signal fidelity, a critical requirement for measurements on thick insulation full-size cables [63]. The measurement cell is shown in Fig. 2.18. In parallel with the hardware development, a dedicated software has been written to manage both data acquisition and signal processing. The acquisition module, which interfaces directly with the oscilloscope, provides full control over key experimental parameters, such as the signals averaging, the definition of the temporal acquisition window, and the number of samples to be recorded. In addition, it allows the user to schedule acquisitions at predefined intervals, ranging from seconds to hours, so that long term monitoring campaigns can be carried out in a fully automated manner. The entire signal processing pipeline, described in

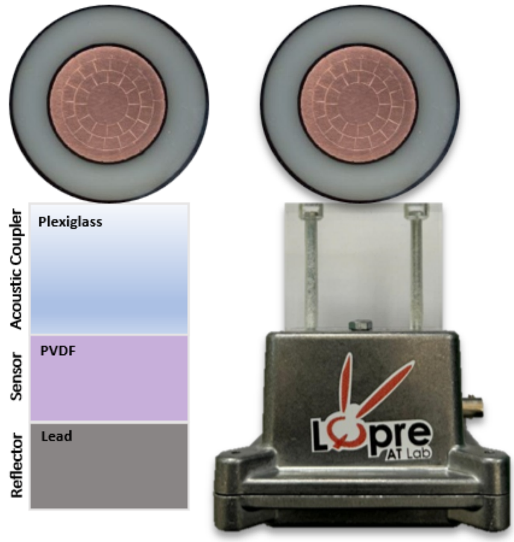

Figure 2.18: PEA cell designed in the L.E.PR.E. laboratory at the University of Palermo.

Section 2.3, together with the acquisition routines, has been implemented with a commercial programming environment. To optimize the analysis, this entire procedure has been organized into a comprehensive Graphical User Interface (GUI), designed to facilitate the application of the multi step corrections and provide immediate visualization of the results (Fig. 2.19 and Fig. 2.20). The implementation and testing of the proposed algorithm have been carried out on a workstation equipped with an Intel Core i7-1165G7 CPU @ 2.80 GHz, 8 GB RAM. Figure 2.21 shows the experimental setup used for PEA measurements on the cable. The cable terminations are connected in a loop, with the voltage applied at the junction point via a high voltage generator. To simulate different load conditions, and therefore different thermal gradients within the insulator, load transformers for inducing current in the cable have been used. At the measurement point, a local cut is made in the outer sheath, creating a window in which the test instrumentation can be placed. The optimization of this diagnostic system followed a process divided into two stages. Initially, the complete measurement chain, comprising the new PEA cell and the custom software, have been thoroughly tested and validated at the L.E.PR.E. HV Laboratory on mini cable samples, as shown in Fig. 2.22. This preliminary phase allowed for the fine tuning of both acquisition parameters and processing algorithms in a controlled environment. Following its validation, the system has been deployed in collaboration with Prysmian for on-site measurements on full-size 525 kV HVDC cables (Fig. 2.23, Fig. 2.24, and 2.25). These tests have been conducted in several high voltage laboratories across Europe, demonstrating the system's robustness, and capability to deliver accurate and reliable space charge measurements in an industrial testing context. Fig. 2.26 shows some of the results obtained during these measurement campaigns.

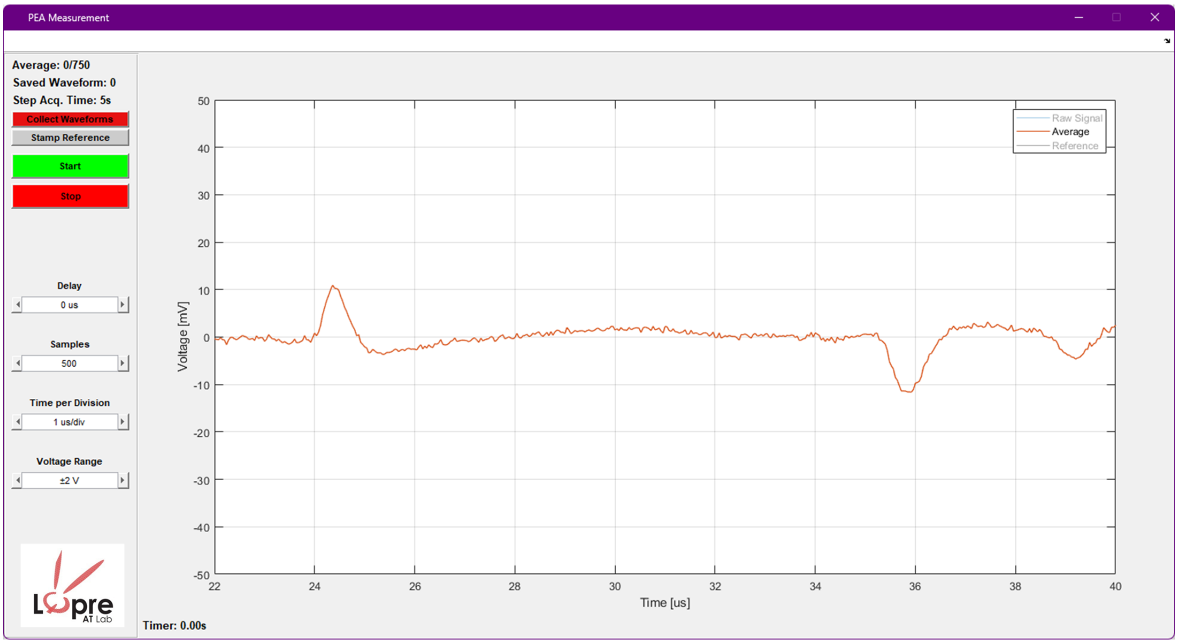

Figure 2.19: Screenshot of the GUI for the raw PEA signal acquisition code

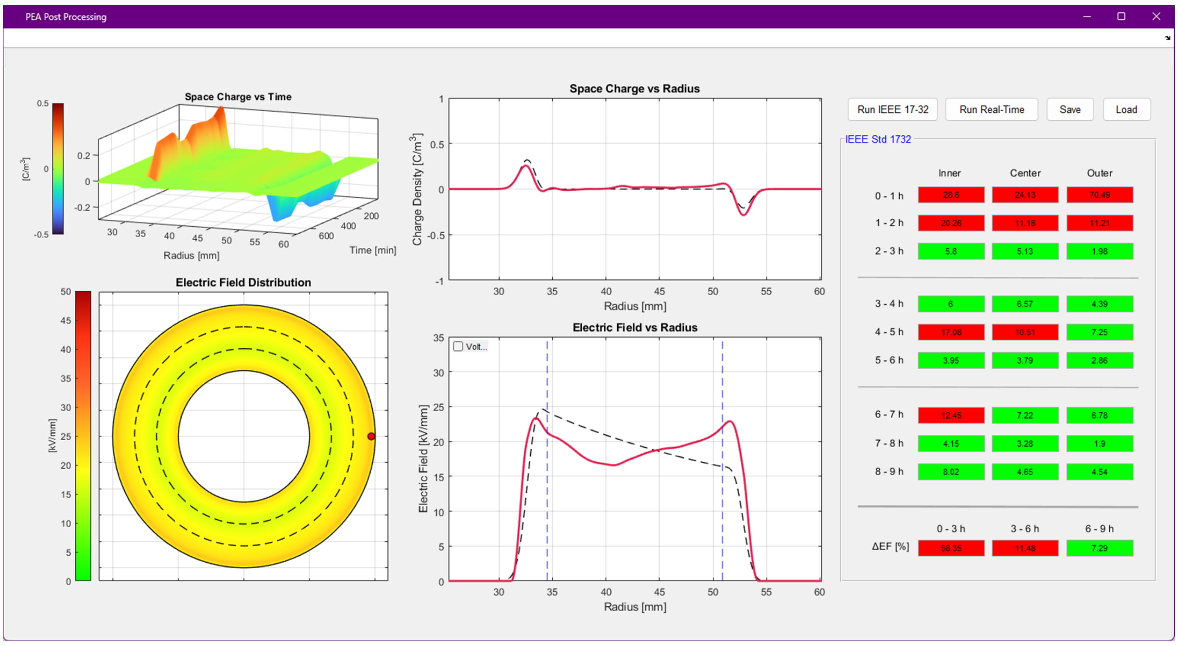

Figure 2.20: Screenshot of the GUI for the raw PEA signal processing code.

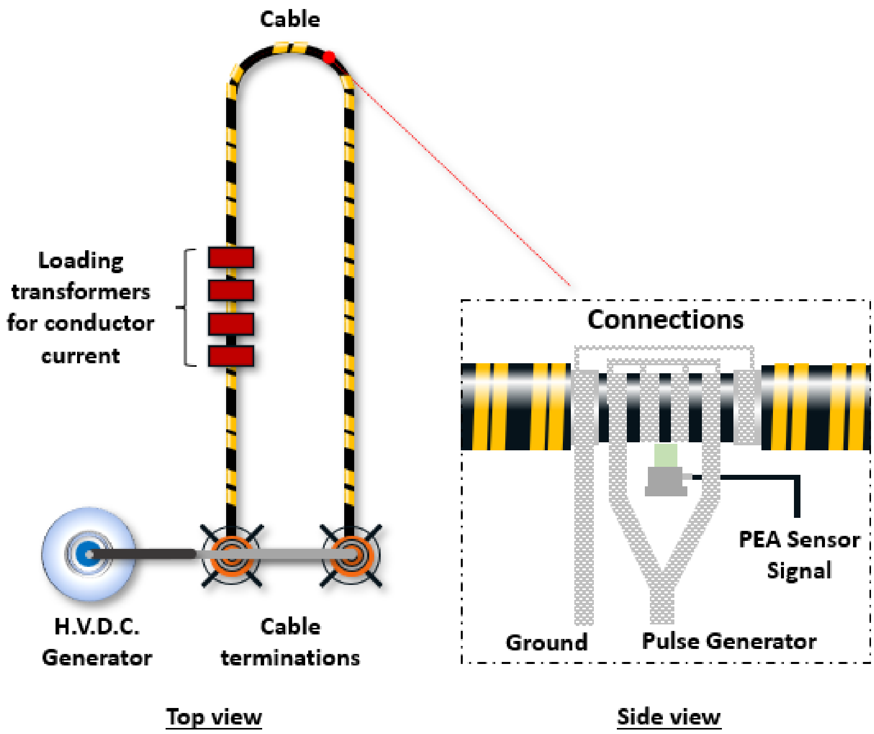

Figure 2.21: Diagram of a PEA setup for measurements on full-size cables.

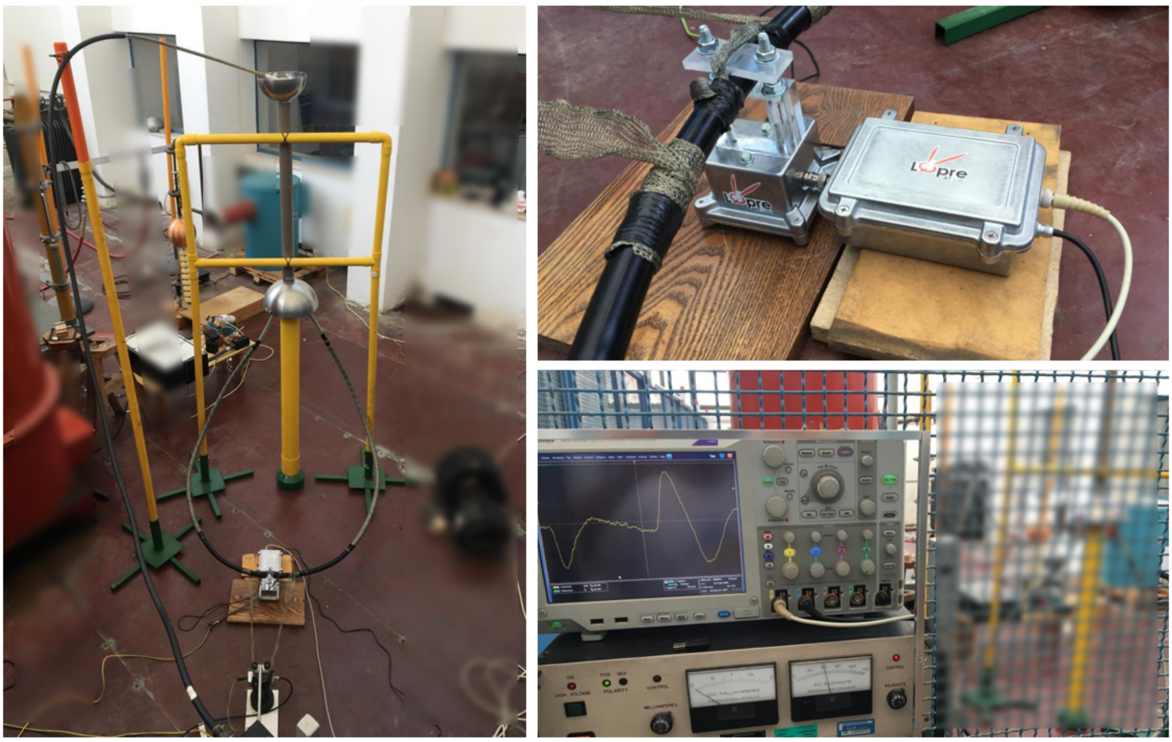

Figure 2.22: Hardware and software testing and validation of the PEA setup for mini cable. Measurement carried out at L.E.PR.E. Lab, Palermo, Italy.

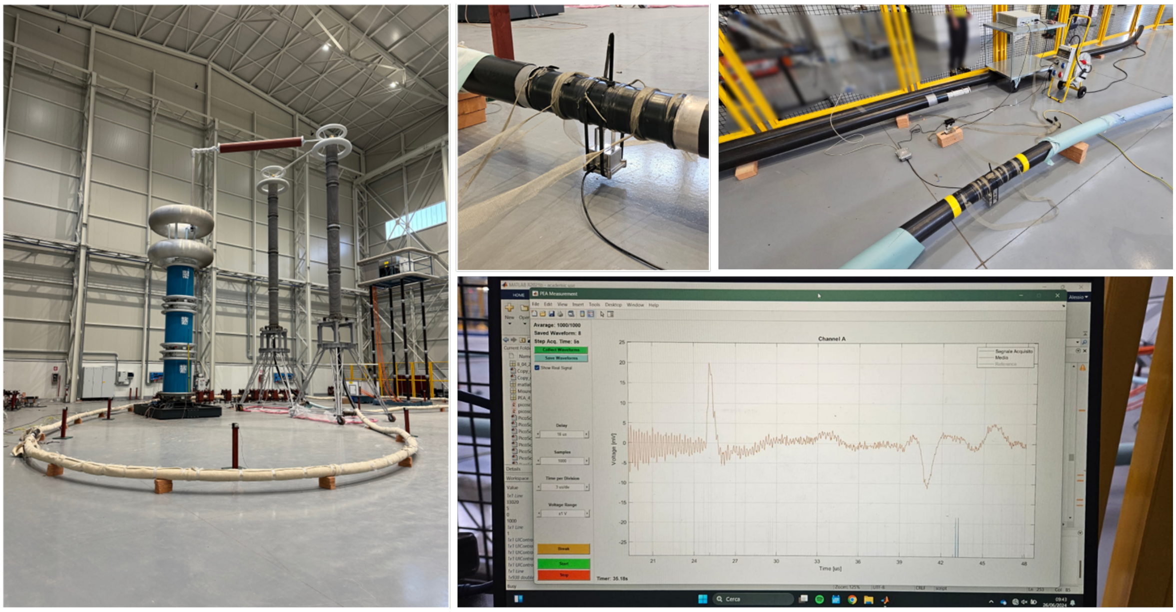

Figure 2.23: Hardware and software testing of the PEA setup for full-size cable. Measurement carried out at Prysmian High Voltage Lab, Quattordio, Italy.

Figure 2.24: Hardware and software testing of the PEA setup for full-size cable. Measurement carried out at Prysmian High Voltage Lab, Montereau, France.

Figure 2.25: Hardware and software testing of the PEA setup for full-size cable. Measurement carried out at Prysmian High Voltage Lab, Bhisopstoke, United Kingdom.

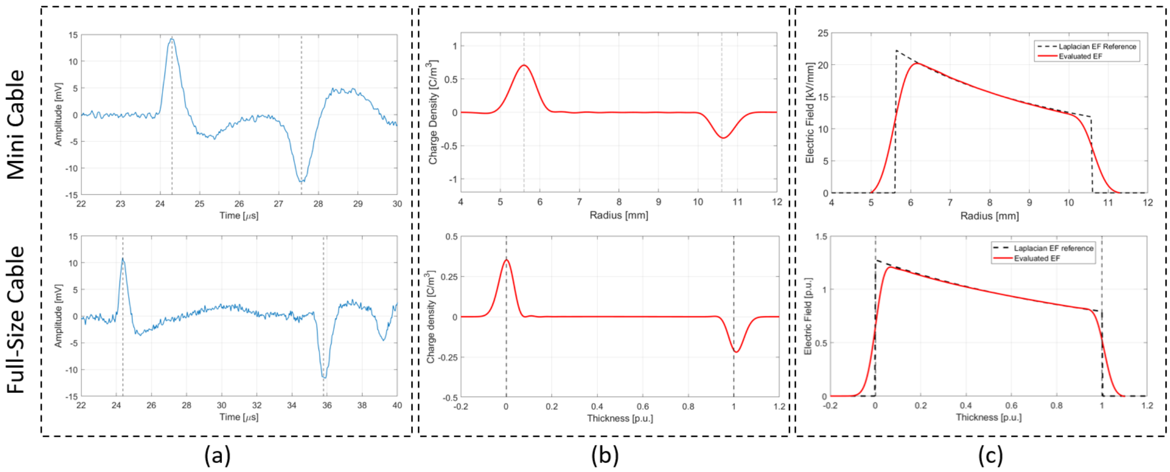

Figure 2.26: PEA measurement results for model and full-size cables. (a) Acquired profiles. (b) Calibrated load profiles. (c) Derived field profiles.

This figure illustrates the three main stages of PEA signal processing. It starts with the raw voltage signal over time (a), acquired by the sensor. After applying the entire processing procedure (which includes deconvolution and several corrections), this is transformed into a quantitative space charge density profile (b). Finally, the electric field distribution (c) is calculated from the latter, which represents the final diagnostic result. The comparison between the measured field (red line) and the theoretical reference (black dotted line) serves to validate the accuracy of the measurement. The tests have been carried out at different voltage levels, ranging from the rated operating voltage up to 1.1 MV. To the best of the authors' knowledge, this represents the first reported implementation of PEA measurements on full-size HVDC cables at voltages exceeding 1 MV, marking a significant milestone for space charge diagnostics under industrial testing conditions.

Chapter 3

A Statistical Methodology for Electric Field Stabilization Assessment

3.1 Electric Field Stabilization as a Reliability Metric

The long term reliability of HVDC cable systems represents a complex engineering challenge that extends far beyond their initial design and manufacturing. Unlike AC systems, the internal electric stress profile of a DC cable is highly dynamic, being continuously influenced by load conditions and operating procedures. The temperature dependent nature of the insulation's conductivity implies that any variation in the load current creates a thermal gradient, which in turn redistributes the electric field. This dynamic behavior makes the assumption of a constant applied voltage an insufficient representation of the stresses experienced in service. Typical operating procedures, such as voltage ramping during energization, controlled shutdowns, and load variations, can significantly influence the internal electric field distribution. Among these, one of the most severe stresses an HVDC cable can face is a polarity reversal. This procedure, which involves reversing the polarity of the applied DC voltage, is sometimes required for operational flexibility, particularly in Line-Commutated Converter (LCC) based systems [64, 65]. A polarity reversal, which may take from 30 seconds to several minutes to be completed, can be extremely adverse to the insulation because the space charge that has accumulated under the previous polarity does not have time to dissipate. Instead, it becomes trapped, and its field superimposes onto the newly applied field of opposite polarity. This superposition can lead to a massive, transient enhancement of the local electric field, potentially exceeding the dielectric strength of the material and triggering a failure [66, 67, 68]. An example of a polarity reversal procedure is shown in Fig. 3.1. Given these severe and

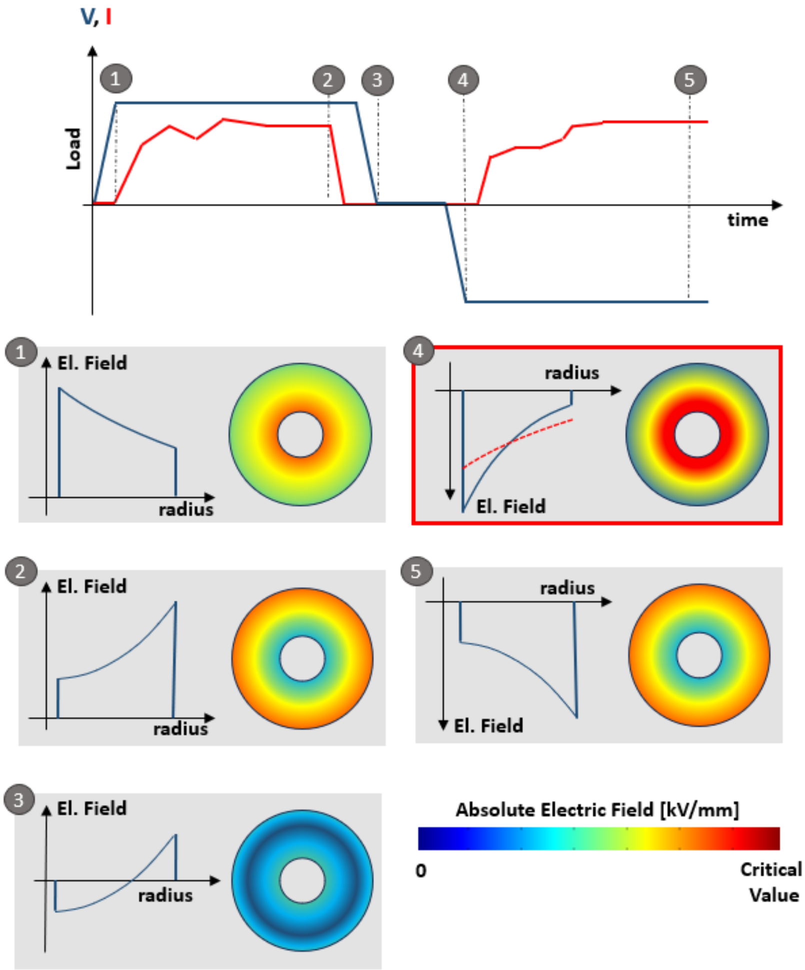

Figure 3.1: Energization procedure (1), electric field inversion (2), voltage cut-off and residual field (3), polarity reversal (4) and new electric field inversion (5).

dynamic operating challenges, from simple load variations to critical events such as polarity reversals, it becomes clear that a static assessment of the insulation state is inadequate. The ability to accurately measure and evaluate the temporal evolution of the electric field profile is not just a diagnostic tool, but a fundamental necessity for ensuring the cable's integrity. Understanding how and how quickly the electric field stabilizes after a change in cable conditions is therefore an important metric for assessing the reliability and operational safety of the entire system. While its full industrial deployment still requires optimization, the PEA method has the potential to provide valuable insights into the dynamic behavior of the insulation, helping to detect critical events, evaluate the effects of load variations and polarity reversals, and ultimately support strategies for ensuring the correct operational management of HVDC cable systems.

3.2 The IEEE Std 1732 Recommendation

The IEEE Std 1732-2017, *"Recommended Practice for Space Charge Measurements on high voltage Direct-Current Extruded Cables for Rated Voltages up to 550 kV"*, provides a standardized framework for evaluating the impact of space charge in HVDC cables [69]. The main objective of the recommendation is to assess the effect of qualification tests on a cable by comparing space charge measurements performed on an unaged sample and an aged sample. The tests are not designed to check for compliance with specific maximum limits, but rather to observe and quantify the temporal variations of the electric field profile derived from PEA measurements. From a hardware perspective, the same setup as in Fig. 2.21 is used. The procedure for assessing electric field stabilization during the test is highly structured and can be summarized in the following key phases [70]:

1. *Cable heating*: by the circulation of a current the conductor is brought to its operating temperature. This step continues until the cable has been subjected to a constant thermal gradient, equal to the designed value, for at least 24 hours. This operation is performed with no voltage applied and is necessary to drain any charge already present in the dielectric. The induced current must be controlled in order to maintain a stable thermal gradient throughout the duration of the test.

2. *Positive volt-on*: application of the rated voltage, with positive polarity, by means of an HVDC generator. From the moment the applied voltage reaches the final (rated) value the PEA measurement can be started ($t = 0h$).

3. *Reference acquisition:* once the PEA measurement has been started, the reference signal must be acquired within five minutes. Through it the parameters for the post-processing will be calibrated.

4. *Profiles acquisition:* a PEA profile is acquired every hour up to a total time of three hours. At the end of the third hour, the charge profiles are processed, and the electric field profiles are derived.

5. *Condition check:* once the field profiles have been obtained, the maximum absolute percentage variation between the field profile at $t = 0h$ and the field profile at $t = 3h$ is evaluated using the following relationship:

$$\Delta E_{max}(0h, 3h) = max\left\{100 \cdot \left|\frac{E_{0h} - E_{3h}}{E_{0h}}\right|\right\} \tag{3.1}$$

The electric field is considered stabilized if the following condition is satisfied:

$$\Delta E_{max}(0h, 3h) \leq 10\% \tag{3.2}$$

If true, the procedure continues directly to step 10. Otherwise, it continues with the next step.

6. *Profiles acquisition:* a second series of PEA profile acquisitions is carried out every hour until a total time of six hours is reached. At the end of the sixth hour, the charge profiles are processed and the electric field profiles are derived.

7. *Condition check:* at the end of this second acquisition interval, the maximum electric field variation between the field profile at $t = 3h$ and the field profile at $t = 6h$ is obtained with the following relation:

$$\Delta E_{max}(3h, 6h) = max\left\{100 \cdot \left|\frac{E_{3h} - E_{6h}}{E_{3h}}\right|\right\} \tag{3.3}$$

The electric field is considered stabilized if the following condition is satisfied:

$$\Delta E_{max}(3h, 6h) \leq 10\% \tag{3.4}$$

If true, the procedure continues directly to step 10. Otherwise, it continues with the next step.

8. *Profiles acquisition:* a third series of PEA profile acquisitions is carried out every hour until a total time of nine hours is reached. At the end of the ninth hour, the charge profiles are processed and the electric field profiles are derived.

9. *Condition check:* at the end of this third acquisition interval, the maximum electric field variation between the field profile at $t = 6h$ and the field profile at $t = 9h$ is evaluated with the following relation:

$$\Delta E_{max}(6h, 9h) = max\left\{100 \cdot \left|\frac{E_{6h} - E_{9h}}{E_{6h}}\right|\right\} \tag{3.5}$$

The electric field is considered stabilized if the following condition is satisfied:

$$\Delta E_{max}(6h, 9h) \leq 10\% \tag{3.6}$$

Even if the condition is not met, the procedure proceeds with step 10.

10. *volt-off test:* after the volt-on test the applied voltage must be removed. The conductor and the metal screen of the cable must be short-circuited. From this moment the volt-off test starts in which a PEA profile is acquired every hour for the following three hours. In this phase no evaluation of percentage variation of the field must be carried out. The recommendation only requires acquiring and reporting the charge and field profiles over the three hours of volt-off.

11. *Rest period:* from the moment the volt-off test ends, a 24-hour interval is considered in which the conductor and the metal screen remain short-circuited.

12. *Negative volt-on:* application of the rated voltage, with negative polarity, by means of an HVDC generator. From the moment the applied voltage reaches the final (rated) value the second PEA measurement can be started ($t = 0h$).

13. Repeat from step 3 to step 10.

The entire procedure is outlined in Fig. 3.2. Although the guidelines provide a solid framework, their practical application, as demonstrated in this thesis, has revealed areas where further refinement may be needed, particularly in relation to the phenomenon of field inversion. The electric field profile typically inverts, shifting the region of maximum stress from the inner to the outer radius of the insulator, within the first hour of the test. This initial and profound change in the field distribution guarantees that the comparison between the $0h$ profile (which is Laplacian) and the $3h$ profile (which is inverted) will almost certainly yield a value far exceeding the 10% threshold. This inherent feature of the physics of space charge accumulation has a direct implication on the test procedure. It effectively forces the volt-on test to continue for a minimum of six hours, regardless of how quickly the field might stabilize after the initial inversion has occurred. This means that, considering the three hours of volt-off, the measurement will last between nine and twelve hours for both polarities. Furthermore, the stability condition is assessed by means of spot measurements taken at three-hour intervals. This procedure makes the result highly dependent on the environmental noise present during the measurement. The latter can derive from various sources (e.g. mechanical and/or electromagnetic) and cause an incorrect interpretation of the field profile status. For these reasons, during the various tests carried out, an alternative procedure for evaluating the stability of the field profile have been also developed, which is presented in the following section.

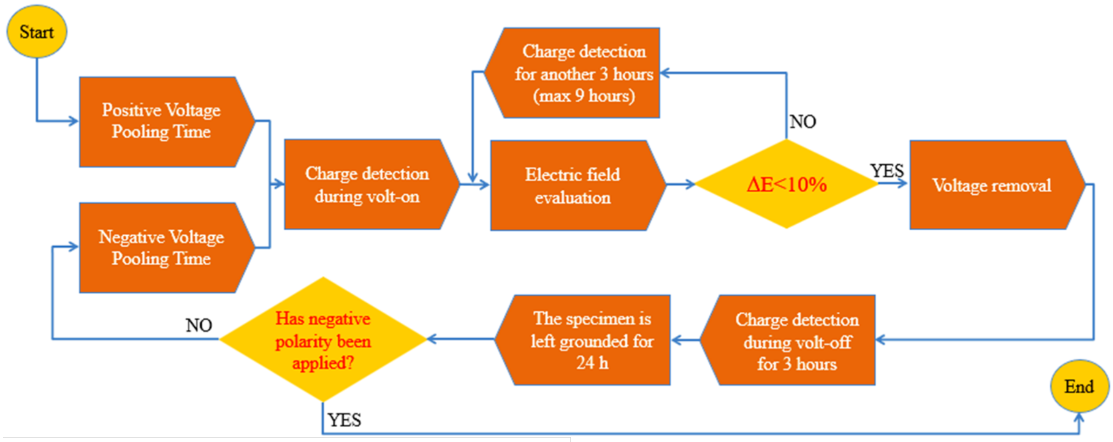

Figure 3.2: Procedure for evaluating the stability of the electric field profile, using PEA measurement, in accordance with IEEE Std 1732 Recommendation.

3.3 Statistical Methodology for Electric Field Stabilization

To overcome the limitations of the spot-check procedure and provide a more detailed understanding of the stabilization dynamics of the cable, this section proposes a statistical methodology. This approach transforms the stability assessment from a simple double-acquisition comparison into a robust trend analysis of a comprehensive dataset, offering a more resilient and representative evaluation of the electric field's dynamic behavior. The key points of the proposed method are as follows:

High-Frequency Data Acquisition: The PEA measurement system is configured to acquire space charge profiles at short, regular intervals (e.g., every 30 seconds) throughout the entire test duration. This generates a rich dataset that captures the continuous evolution of the insulation's dielectric state, rather than just isolated snapshots in time.

Temporal Evolution of ΔE_{max}: For each analysis interval ($0h - 3h$, $3h - 6h$ and $6h - 9h$), a time series of ΔE_{max} is evaluated. Each point in this series represents the maximum field variation between the currently acquired profile (E_i) and the reference profile taken at the beginning of that specific interval (E_{ref}) according the following equation:

$$\Delta E_{max}(i) = max\left\{100 \cdot \left|\frac{E_{ref} - E_i}{E_{ref}}\right|\right\} \tag{3.7}$$

Rather than summarizing this time series by means of a single indicative value, which could be misleading in the presence of fluctuations or transient disturbances, the proposed methodology relies on a set of statistical indicators that collectively provide a richer picture of the system's behavior. To provide a more robust characterization of the field variations, it has been decided to rely on two pairs of statistical indicators. The first pair, consisting of the mean and standard deviation, captures the overall trend and the dispersion of the data, offering insight into the general behavior and consistency of the stabilization process. The second pair, comprising the median and the Inter-Quartile Range (IQR), provides a complementary, more robust perspective that is less sensitive to transient disturbances or outliers, allowing a reliable assessment of the central tendency and variability within the most representative portion of the data. By combining these two pairs, the statistical framework offers a robust and sensitive approach for assessing the electric field stabilization. By simultaneously considering both the central tendency, through the mean and median, and the dispersion, via the standard deviation and IQR, the method effectively mitigates the impact of random noise and transient fluctuations. Consequently, the evaluation of stability reflects the overall dynamic behavior of the system within the observation window, rather than being influenced by isolated anomalous measurements, providing a more reliable and representative characterization of the electric field's true evolution. During some of the tests carried out to validate the hardware and software components of the PEA setup, a measurement has been performed following the IEEE 1732 recommendation. By increasing the number of acquisitions every thirty seconds, it was possible to compare the results with those obtained using the statistical approach presented in this section. The comparison is discussed in the following section.

3.4 Experimental Validation on a 525 kV Extruded Cable

The proposed statistical methodology has been applied to the dataset obtained from a PEA measurement performed on a full-size 525 kV extruded HVDC cable. The test has been carried out in full accordance with the IEEE 1732 procedure, providing a direct opportunity to compare the results of the statistical framework with the traditional spot-check approach on an industrially relevant test case. The results reported in Table 3.1 indicate a stabilization process that has been completed by the ninth hour for the positive volt-on measurement ($+U_0$) and by the sixth hour for the negative volt-on measurement ($-U_0$). Fig. 3.3 and Fig. 3.4 depict the electric field profiles derived from the processed PEA signals for both tests. For confidential reasons, the field profiles are reported on per unit basis, using the mean electric field, $E_m = U_0/d$, as the base quantity. These results clearly show the large percentage

Time Intervals	ΔE_{max} for $+U_0$	ΔE_{max} for $-U_0$
$0h - 3h$	60.7%	67.4%
$3h - 6h$	12%	7.8%
$6h - 9h$	7.5%	-

Table 3.1: Test results according to IEEE std 1732 Recommendation. Field stabilization achieved with values below 10%.

variation during the first measurement interval ($0h - 3h$) due to the field inversion. In the subsequent intervals, the difference between the profiles is significantly reduced. However, these individual values are not sufficient to fully describe the information acquired during the measurement. The left panel of Fig. 3.5 shows the trend of ΔE_{max} during the positive volt-on test, evaluated across the three measurement intervals defined in Eq. 3.7. In the first interval ($0h-3h$), the inversion of the field profile within the first half hour is clearly observed, followed by a settlement around an average value, although characterized by large fluctuations. In the next two intervals, the average value is lower, but the strong dispersion remains, highlighting the intrinsic unreliability of spot measurements, which coincide with the last value of the trends represented. In the interval $6h-9h$, there is also a spike attributable to a fluctuation in the applied voltage. If a disturbance of this type, even of a smaller magnitude, were to occur near the end of one of the intervals, the measurement would inevitably be affected, resulting in an alteration of the data obtained. To refine the analysis, the observed trends were further discretized into one-hour intervals, as illustrated on the right panel of Fig. 3.5. This choice is motivated by considerations related to the measurement procedure. According to IEEE 1732, the cable should be pre-heated prior to voltage application and test initiation. However, this condition is not practically feasible, as it would imply energizing a cable already operating

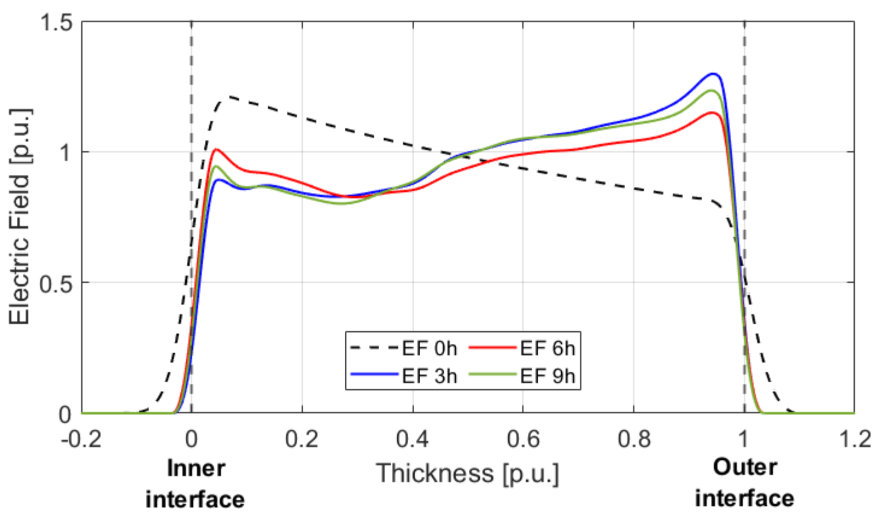

Figure 3.3: Electric field profile for positive volt-on test.

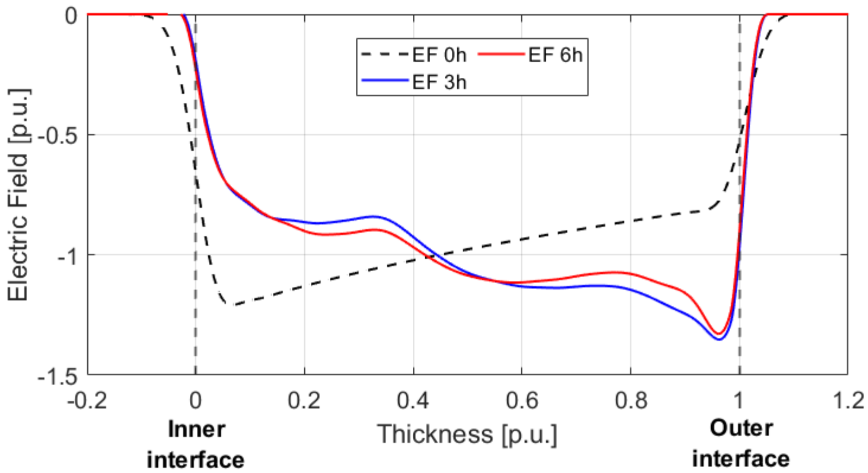

Figure 3.4: Electric field profile for negative volt-on test.

at full load. Moreover, both the temperature gradient and the energization phase induce a rapid field inversion process, making the electric field behaviour highly dynamic. Under these circumstances, it becomes particularly evident that data variability is strongly time dependent, being very pronounced in certain intervals and much lower in others (e.g., in the interval $3h-4h$). Fig. 3.6 shows the box plots relating to the ΔE_{max} trends obtained during

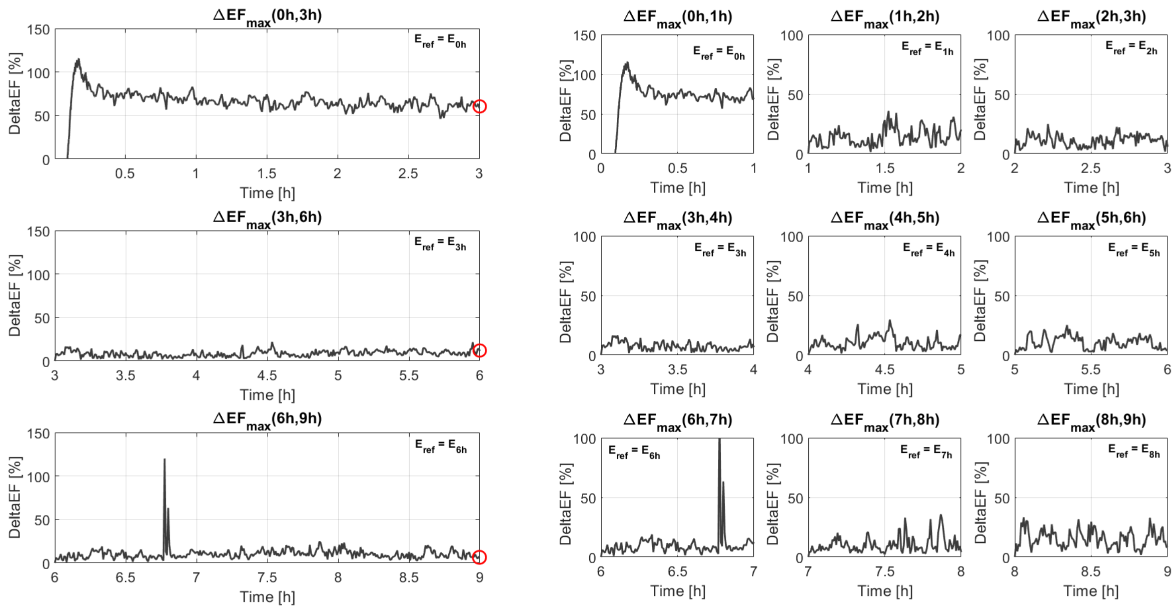

Figure 3.5: Time trend of ΔE_{max} for the positive volt-on test evaluated over three-hour intervals (left) and over one-hour intervals (right). The red circles highlight the single value considered in the assessment according to IEEE 1732.

the positive volt-on test, while Table 3.2 shows the mean values and standard deviations calculated for the same trends. The analysis revealed significant insights into the stabilization dynamics. By evaluating the data in one-hour intervals, it was possible to track the process with high temporal resolution. After the initial, highly variable period dominated by field

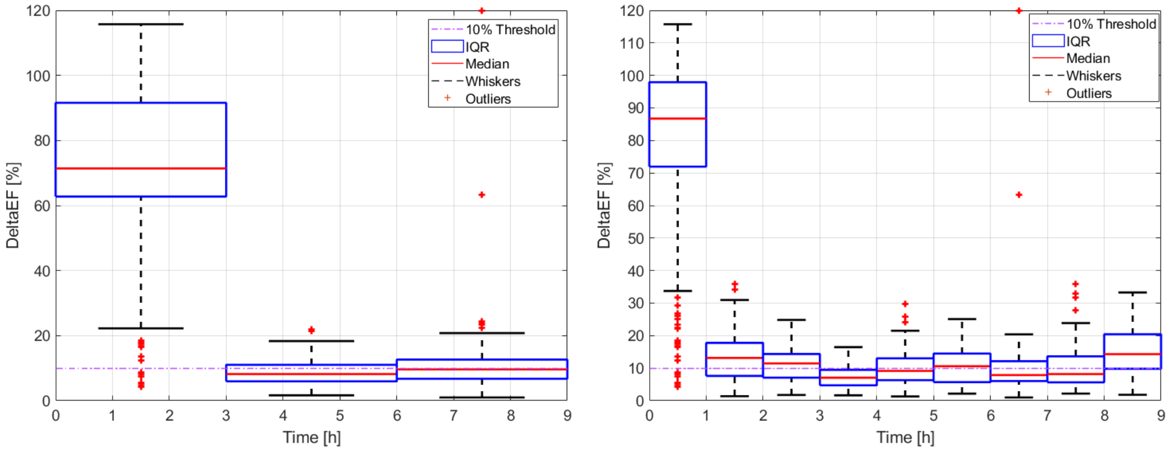

Figure 3.6: Box Plot for the trend reported in Fig. 3.5.

inversion, the system's fluctuations decrease markedly. The stabilization condition, defined as the median and IQR of ΔE_{max} falling below the 10% threshold, was reliably met during the fourth hour of the test, with a mean variation of just 7.38%. This indicates that the insulation system had reached a quasi-steady state at this point. In contrast, an analysis based on the standard three-hour intervals would have led to a different conclusion. In that case, the stabilization condition was only met at the end of the second interval, i.e., at the six-hour mark, with a mean variation of 8.49%. Furthermore, the two point spot-check method prescribed by the IEEE 1732 standard detected a stabilization stage after nine hours of measurement. During the negative volt-on test, whose stabilization has been completed at the end of the sixth hour according to IEEE 1732, the trends shown in Fig. 3.7 have been calculated. Fig. 3.8 shows the box plots obtained from the analysis at three-hour and one-hour intervals, respectively. The result obtained is particularly significant, since according to this distribution the condition of stability of the electric field at the end of the sixth hour has not been reached. Observing the trends with one-hour time ranges, it can be seen that, apart from the first hour, the median values of ΔE_{max} do not fall below the 10% threshold, although they remain close to it. The only exception is represented by the box plot corresponding to the fourth hour, where a considerable increase in the variability of the data is observed. Table 3.3 reports the mean values and standard deviations for all the time ranges considered in the negative volt-on test. From these data, it is difficult to conclude that a stable electric field condition has been achieved, since none of the average values falls below the 10% threshold. These results demonstrate that the statistical approach allows for obtaining a greater amount of information on the dynamics of the observed phenomenon. Data fluctuations due to background noise are taken into account, and the choice to use one-hour or three-hour intervals allows for a clearer picture of rapid and slow processes, respectively. More accurate recognition of the

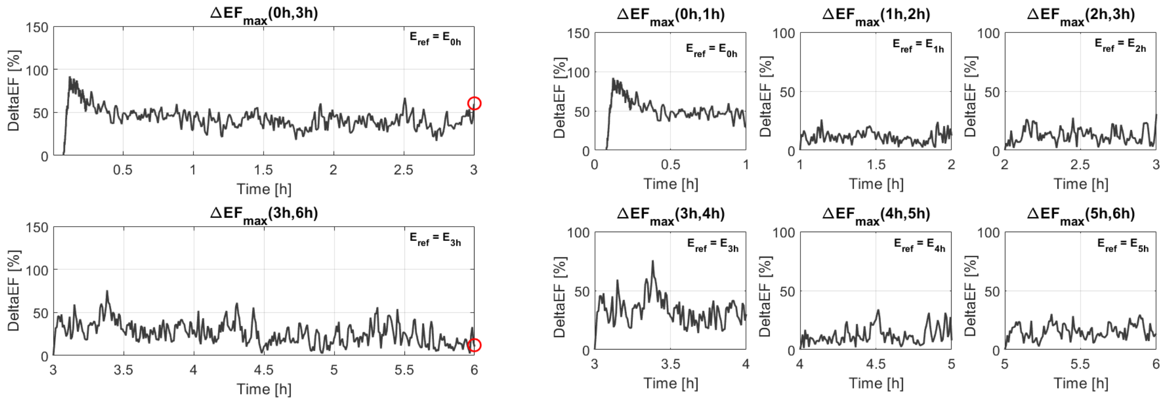

Figure 3.7: Time trend of ΔE_{max} for the negative volt-on test evaluated over three-hour intervals (left) and over one-hour intervals (right). The red circles highlight the single value considered in the assessment according to IEEE 1732.

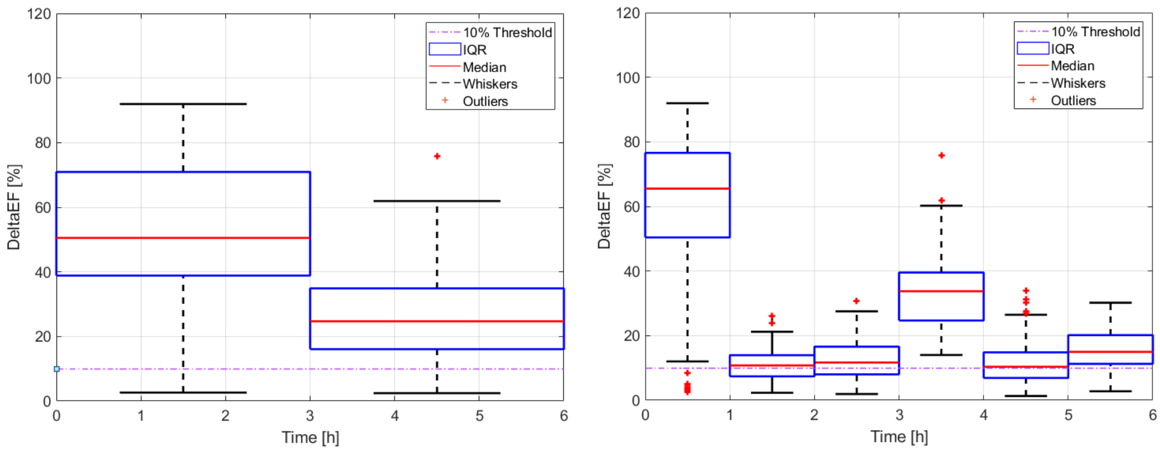

Figure 3.8: Box Plot for the trend reported in Fig. 3.7.

stabilization condition would help to avoid excessively long measurement times, making the integration of this type of test in a high voltage laboratory more efficient.

Time Interval		$\mu_{\Delta E} \pm \sigma_{\Delta E}$	
0h-1h	**0h-3h**	87.12% ± 16.58%	76.73% ± 18.55%
1h-2h		13.79% ± 6.91%	
2h-3h		11.12% ± 4.85%	
3h-4h	**3h-6h**	7.38% ± 3.48%	8.49% ± 3.46%
4h-5h		9.87% ± 4.76%	
5h-6h		10.51% ± 5.37%	
6h-7h	**6h-9h**	8.68% ± 3.99%	9.88% ± 4.14%
7h-8h		9.27% ± 5.14%	
8h-9h		15.43% ± 7.44%	

Table 3.2: Mean values and standard deviations of ΔE_{max} for positive volt-on test.

Time Interval		$\mu_{\Delta E} \pm \sigma_{\Delta E}$	
0h-1h	**0h-3h**	63.20% ± 17.14%	53.18% ± 19.54%
1h-2h		10.86% ± 4.48%	
2h-3h		12.49% ± 6.05%	
3h-4h	**3h-6h**	32.77% ± 10.71%	25.99% ± 12.77%
4h-5h		11.06% ± 5.86%	
5h-6h		15.46% ± 6.10%	

Table 3.3: Mean values and standard deviations of ΔE_{max} for negative volt-on test.

Chapter 4

Advanced Separation and Analysis of Partial Discharge Phenomena in DC

4.1 The Partial Discharge Phenomenon

Partial Discharges (PD) are localized dielectric breakdowns that occur within a small portion of an insulation system when the local electric field exceeds the breakdown strength of the material, without completely bridging the space between two electrodes [71]. Unlike a full breakdown, which results in a permanent short circuit, PD are transient events that release only a limited amount of energy. Nevertheless, their repetitive occurrence gradually deteriorates the insulation, leading over time to failures in high voltage equipment [72]. A PD source can be obtained in the presence of structural defects in the volume or on the surface of a solid dielectric. In the first case, small cavities or gas inclusions within the material can generate intense local electric field reinforcements, promoting the triggering of internal discharges. In the second case, surface imperfections, uneven contacts or contamination can lead to the formation of creeping discharges along the solid-air or solid-solid interface. A further category is represented by corona discharges, which develop in gaseous media around conductive edges or points subjected to a strong electric field gradient. The detection of PD is typically carried out by monitoring the fast current or voltage impulses they generate, either directly through electrical measurements or indirectly using acoustic, optical, or electromagnetic sensors [73, 74, 75]. Among these, electrical detection remains the most widely adopted technique due to its sensitivity and compatibility with standardized procedures. However, electrical methods generally require the direct connection of measuring devices to the circuit in which the Device Under Test (DUT) operates. An alternative to conventional electrical detection techniques is the use of Ultra-Wide Band (UWB) antenna sensors. These sensors capture the electromagnetic emissions produced by PD without the need to insert any measurement device into the high voltage circuit. Due to their broad frequency response, UWB antennas are able to detect the fast transient signals associated with PD activity, providing both high sensitivity and temporal resolution [76]. By capturing the characteristic pulses associated with PD activity, it becomes possible to not only confirm the presence of insulation defects but also to extract information about their origin and severity. From a diagnostic point of view, PD are of critical importance as they serve both as indicators of existing defects and as early warnings of potential insulation breakdown. Detecting and analyzing these phenomena provides essential information on the health of high voltage assets, enabling timely identification of weaknesses, focused maintenance interventions, and a reduced risk of major failures. Consequently, PD monitoring has established itself as a key element in modern approaches to condition assessment and lifetime management of power cables, transformers, rotating machines, and other high voltage equipment [77].

4.2 The Challenge of PD Analysis Under DC Voltage

While PD detection and analysis are well established for AC systems, the diagnosis of PD in HVDC applications presents unique and significant challenges that require a fundamental shift in analytical approach. The core of the problem lies in the different physical mechanisms governing the insulation's behavior under AC versus DC stress [78]. In AC systems, the dielectric behavior is dominated by its capacitive properties. The electric field distribution is stable and determined by the material's permittivity, and the discharge activity is cyclically linked to the sinusoidal voltage waveform. This deterministic relationship allows for the use of the Phase-Resolved Partial Discharge (PRPD) pattern as the cornerstone of diagnostics. The PRPD pattern plots the discharges magnitude against the phase angle of the AC cycle, creating distinct ”fingerprints” that are often sufficient to identify the type of PD source (e.g., corona, internal void, surface discharge) with high confidence [79]. This approach becomes invalid under DC conditions. The system is no longer governed by capacitance but by the resistive properties of the insulation. The electric field distribution is not static, it is dynamically influenced by the material's conductivity, which in turn is highly dependent on local temperature and electric field strength. Consequently, the occurrence of discharges becomes a more stochastic process, driven by complex interactions between local field conditions, space charge accumulation, and thermal gradients, rather than a simple

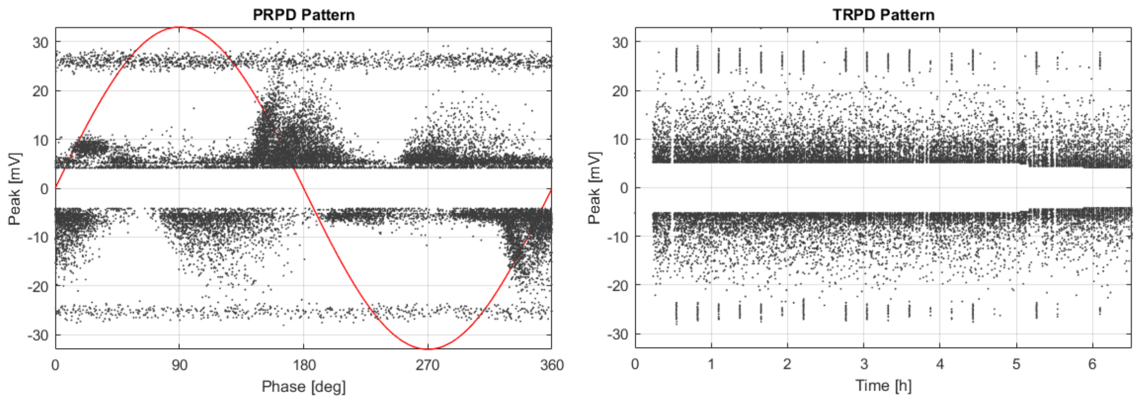

Figure 4.1: Comparison between PRPD and TRPD patterns. It can be seen how the distribution with respect to the sine wave allows the nature of the discharge phenomenon to be determined based on the phase reference.

relationship with the applied voltage. The most profound consequence of this shift is the complete absence of a phase reference, rendering the powerful PRPD pattern unusable. Without this tool, it becomes incredibly difficult to distinguish between different types of PD phenomena occurring simultaneously, or to separate genuine discharge signals from background noise and other electromagnetic disturbances. A possible alternative is to use the Time-Resolved Partial Discharge (TRPD) pattern, which, however, only provides a temporal distribution of discharge events but does not allow any speculation on their nature. A comparison between PRPD and TRPD patterns is shown in Fig. 4.1. This difficulty is compounded by the lack of a standardized procedure or reference for the recognition and classification of PD in HVDC systems. These challenges necessitate the development of new, more sophisticated analysis techniques [80, 81, 82]. The focus must shift away from the relationship between the discharge and the supply voltage, and towards methods that can extract meaningful information directly from the intrinsic characteristics of the acquired pulses themselves, such as their time domain waveforms and frequency content. This is the fundamental motivation for the separation strategies and visualization algorithms developed and presented in the following sections.

4.3 Separation by Cross-Correlation Clustering

To overcome the inherent limitations of PD analysis in the DC domain, a novel analytical approach have been developed. Instead of attempting to find a substitute for the phase reference, this methodology focuses on extracting information directly from the intrinsic characteristics of the individual discharge pulses. The core principle is that pulses originating from the same physical phenomenon, and propagating through the same path to the sensor, should exhibit highly similar time domain waveform shapes. By quantifying this similarity, it becomes possible to group the acquired pulses into distinct families, each corresponding to a specific PD source or type of noise. The mathematical tool chosen to rigorously measure this waveform similarity is the cross-correlation [44]. Given two signals in the time domain, $x_1(t)$ and $x_2(t)$, the cross-correlation evaluates the degree of overlap between them as one signal is shifted in time (τ) relative to the other, as described by the following integral.

$$R(\tau) = \int_{-\infty}^{\infty} x_1(t) \cdot x_2(t+\tau) dt \tag{4.1}$$

The maximum value of $R(\tau)$, defined as correlation coefficient (k_{cc}), corresponds to the point of best alignment and quantifies the highest degree of similarity between the two waveforms. By normalizing the two functions with respect to their energy, and by considering the absolute value, k_{cc} is conveniently scaled to a range between 0 (indicating no correlation) and 1 (indicating identical shape), providing a consistent and objective metric [83]. This approach is fundamentally more powerful than methods based on a few extracted features (e.g., peak amplitude, rise time) because it is sensitive to the entire morphology of the pulse. It considers the complete shape, including oscillations, damping, and duration, which are all part of the unique signature of a specific discharge phenomenon. This comprehensive comparison makes it highly effective for distinguishing between different types of discharges whose characteristics might otherwise appear similar when reduced to a small set of parameters. An additional optimization in the computation of the correlation coefficient relies on the use of the Fourier transform $\mathcal{F}(\cdot)$. Instead of directly evaluating the correlation integral in the time domain, the Fourier transforms of the signals can be exploited to accelerate the process. According to the convolution theorem, the cross-correlation between two signals can be obtained in the frequency domain by multiplying the spectrum of one signal with the complex conjugate of the spectrum of the other:

$$\mathcal{F}\{R(\tau)\} = \mathcal{F}\{x_1(t)\} \cdot \overline{\mathcal{F}\{x_2(t)\}} \tag{4.2}$$

This property makes it possible to compute the cross-correlation via a simple multiplication followed by an inverse Fourier transform, reducing the computational complexity from the order of $O(N^2)$ to $O(N \log N)$ thanks to the use of fast Fourier transform algorithms. Such an approach is particularly advantageous when dealing with large datasets or long acquisition windows, where direct time domain evaluation would otherwise be computationally prohibitive. The cross-correlation based separation has been implemented through two complementary algorithms, each tailored to different application requirements. The first one is optimized for real time operation: it is computationally lighter and capable of providing immediate feedback during acquisition, though at the expense of some accuracy in waveform comparison. The second algorithm, instead, is designed for post-processing: by exploiting more refined calculations and broader data availability, it achieves higher precision in clustering and discrimination of PD sources, even though with longer processing times. This dual implementation ensures both the possibility of on-line monitoring during tests and the availability of an in-depth, high-resolution analysis once the data have been acquired.

4.3.1 PD Separation Algorithm #1

The first algorithm is designed for computational speed, making it suitable for on-line monitoring and real-time analysis. It operates by processing pulses sequentially as they are acquired. The operational flow of this semi-automatic method is illustrated in the block diagram in Fig. 4.2. The process begins when a new pulse is acquired. Instead of being compared to every previously recorded pulse, it is compared only to a small set of reference signals. Each reference signal is a representative waveform for an already-established cluster and is dynamically updated as new pulses are assigned to it. This reference is typically calculated as the weighted average of all pulses within that cluster, giving more weight to signals with higher amplitude to reduce the influence of noise. The new pulse is then assigned to the cluster whose reference signal yields the highest correlation coefficient. However, this assignment only occurs if the coefficient exceeds a user-defined threshold. If the highest correlation value falls below this threshold, it is assumed that the pulse belongs to a new, previously unidentified phenomenon, and a new cluster is created with this pulse as its first member. In a numerical sense, therefore, the algorithm constructs a matrix in which each row refers to a cluster and the columns identify the indices of the pulses belonging to that family of signals. The main advantage of this sequential approach is its computational efficiency, which makes it a viable candidate for providing immediate feedback during long measurement sessions. However, its performance is inherently less robust. The final clustering result is dependent on the order in which the pulses are acquired and is sensitive to the user-selected threshold, making the algorithm semi-automatic and its results potentially less precise than a holistic, offline analysis.

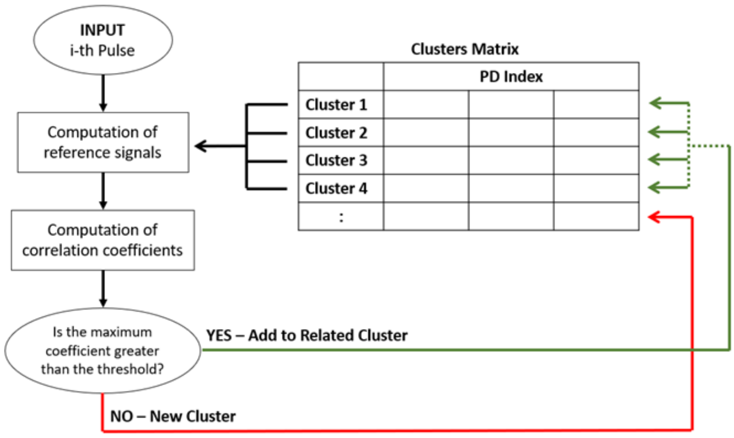

Figure 4.2: Block diagram of algorithm #1 for PD separation using cross-correlation.

4.3.2 PD Separation Algorithm #2

The second algorithm is designed for maximum accuracy and robustness, intended for detailed, offline post-processing of the complete acquired dataset. It is a fully unsupervised and automatic method that leverages the full informational content of the data to achieve a more physically meaningful partitioning. The process, visualized in the block diagram of Fig. 4.3, is fundamentally different from the sequential approach. The first step is the computation of the complete cross-correlation matrix, M_{CC}, by cyclically applying the following operation:

$$M_{CC}(i,j) = \max_{\tau} \left| \int_{-\infty}^{\infty} x_i(t) \cdot x_j(t+\tau)\, dt \right|, \qquad i,j = 1,2,\ldots,n \tag{4.3}$$

This nxn matrix, where n is the total number of pulses, contains the similarity measure between every possible pair of waveforms in the dataset. The algorithm then uses this matrix as the input for a standard hierarchical clustering routine [84]. Since hierarchical clustering algorithms require as input a distance matrix rather than a similarity matrix, a transformation of the cross-correlation results is necessary. In fact, hierarchical methods operate by progressively merging or splitting groups of data points based on their mutual distances, which are then represented in a tree-like structure known as a dendrogram. In the map used to represent the data, distances provide a natural geometric interpretation: two points are close (similar) if their distance is small, and far apart (different) if their distance is large. Conversely, the cross-correlation matrix expresses similarity, where higher values indicate greater resemblance between waveforms. To reconcile this difference, the similarity values are converted into distances by taking their complement to unity, $M_D = |1 - M_{CC}|$. In this way, two signals with very high correlation (close to 1) yield a distance close to 0, meaning

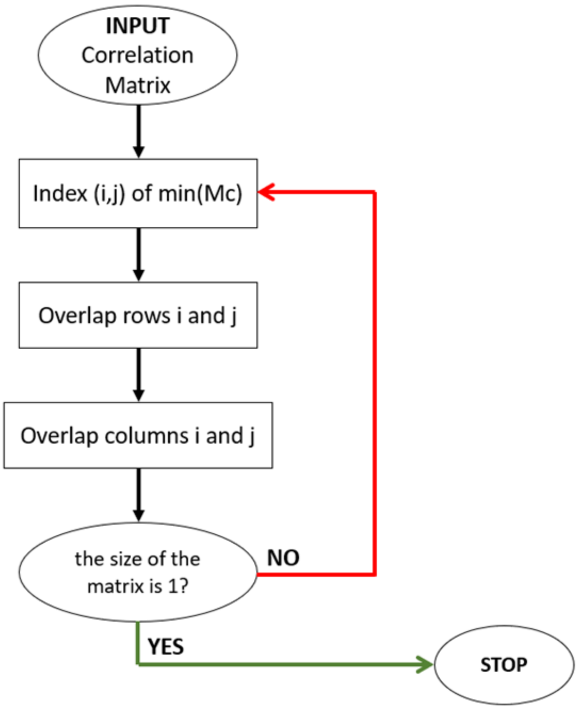

Figure 4.3: Block diagram of algorithm #2 for PD separation using cross-correlation.

they will be grouped together early in the clustering process, while less correlated signals will appear farther apart in the distance map. This transformation enables the direct application of hierarchical clustering on the cross-correlation results, ensuring that the partitioning of the dataset reflects the intrinsic proximity relations between the discharge waveforms. The implemented algorithm proceeds agglomeratively: it begins by treating each individual pulse as a separate cluster. In each subsequent step, it identifies the two most similar clusters by finding the minimum value in the matrix M_D and merges them into a new, larger cluster. This iterative merging process continues until all pulses are grouped into a single hierarchical structure, which can be visualized as a dendrogram. The primary advantage of this method is its high accuracy. By considering the relationships between all pulses simultaneously, it produces a stable and objective result that is not dependent on the acquisition order or user-defined parameters. Its main limitation lies in the significant computational cost and memory demand required to calculate and store the complete correlation matrix, whose size grows quadratically with the number of pulses. For large datasets, this scaling rapidly becomes prohibitive, as both the correlation evaluation and the subsequent clustering require handling millions of pairwise comparisons. These constraints make the method unsuitable for real-time implementation, where rapid feedback and limited hardware resources are critical.

4.4 Validation and Comparison of the Two Algorithms

To validate their performance and compare their effectiveness, both the sequential and the hierarchical clustering algorithms have been tested on a PD dataset acquired during a laboratory measurement on an XLPE model cable subjected to DC voltage stress of 70 kV. An artificial defect has been made on the cable to simulate the presence of a cavity between the dielectric and the outer semiconductive layer. The measurement has been carried out with the Pry-cam, a PD detection device consisting of an UWB spherical antenna sensor combined with a digital acquisition system with a sampling frequency of 200 MS/s. The total resulting bandwidth of the instrument is 0.5–100 MHz [76]. A photo of the setup is shown in Fig. 4.4. To allow a direct qualitative comparison, the separation results were represented on a Time-

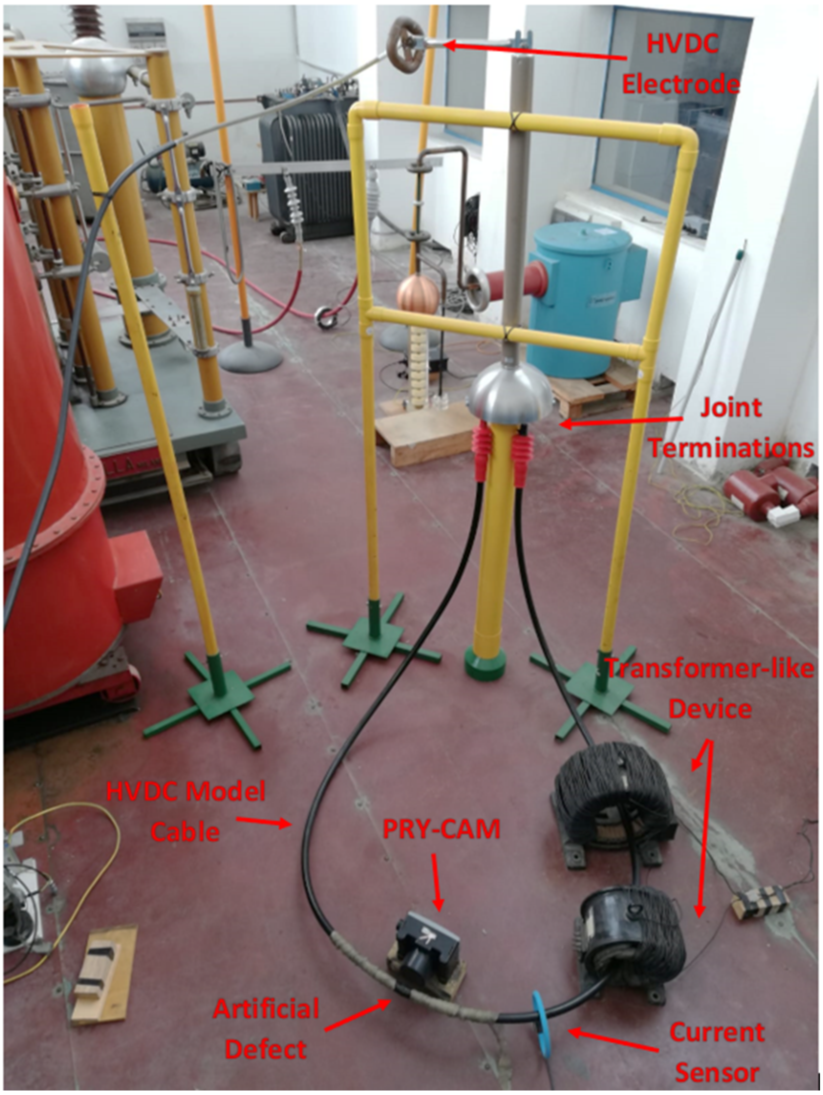

Figure 4.4: Setup for PD measurement in XLPE model cable with artificial defect.

Frequency (TF) map. Each PD pulse is characterized in both time and frequency domains, with the information condensed into the Equivalent Timelength (T) and Equivalent Bandwidth

(F) [85]. Each pulse is then plotted as a single point on this 2D map. This visualization is particularly useful in DC analysis as it can reveal inherent structures or patterns within the data. In this context, the TF map serves as a canvas. After the algorithms partitioned the dataset based on waveform similarity, each pulse on the map was colored according to the cluster it was assigned to. The results of this process are shown in Fig. 4.5. A direct comparison of the two maps reveals several key insights. Both algorithms successfully identify the main underlying phenomena present in the dataset, partitioning the pulses into distinct colored groups. However, the hierarchical algorithm (right map) provides a significantly cleaner and more precise separation. It is particularly effective at resolving clusters whose patterns are partially overlapping in the TF map, correctly grouping them based on their intrinsic waveform similarity, even when their points are overlapped in this specific 2D representation. In contrast, the sequential algorithm (left map), while still able to identify the general structure of the data, exhibits some misclassifications at the boundaries between adjacent clusters, as evidenced by the less defined separation between the colored groups. This lower precision is an inherent consequence of its methodology. The figure clearly illustrates the fundamental trade-off between the two methods: the hierarchical algorithm delivers superior accuracy and robustness, making it ideal for detailed post-analysis, while the sequential algorithm offers a faster, computationally lighter alternative at the cost of reduced precision, making it more suitable for preliminary or real time applications. Despite the observed differences in their accuracy, it is crucial to emphasize a fundamental strength that both the sequential and the hierarchical algorithms share. Their common foundation on the cross-correlation metric allows them to overcome the primary limitations often encountered with traditional clustering algorithms like k-means, DBSCAN, or the classic hierarchical method based on a distance matrix as shown in Fig. 4.6. The key advantage is that by operating on the principle of waveform similarity rather than spatial proximity in a feature map, both proposed methods are capable of successfully separating clusters with diverse shapes and varying densities. Most importantly, they can effectively resolve partially overlapping patterns, a common scenario in PD analysis that often leads to misclassification by conventional algorithms. This demonstrates that the shift from a feature space distance approach to a direct waveform similarity approach represents a significant step forward in the robust and accurate separation of partial discharge sources in DC.

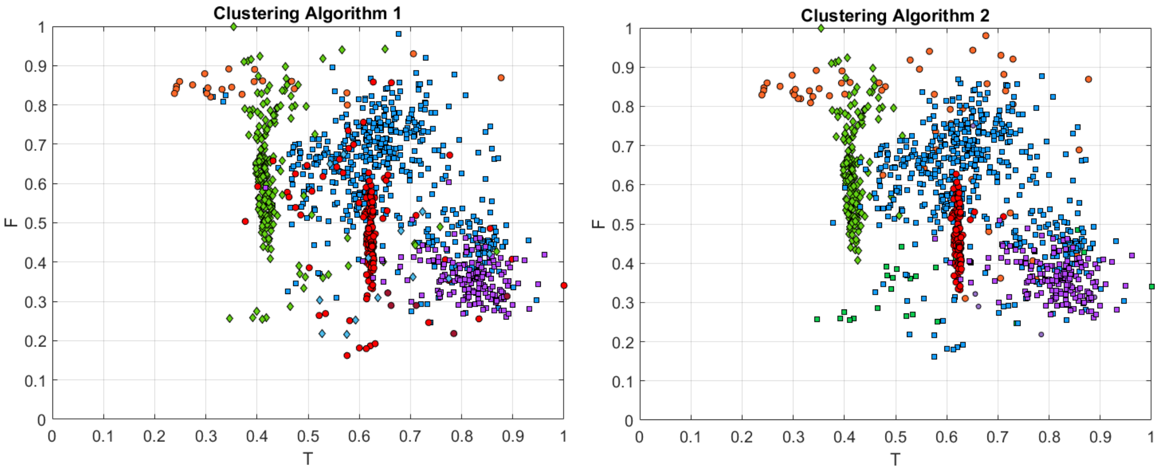

Figure 4.5: TF maps clustered with the two cross-correlation-based algorithms

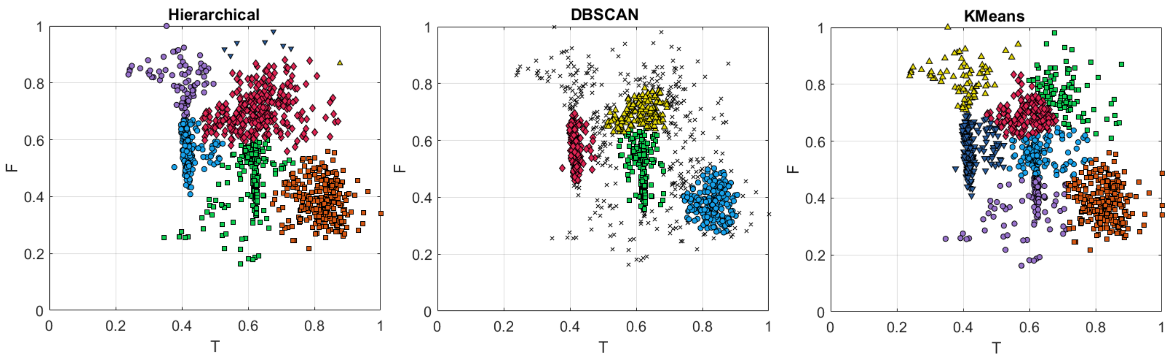

Figure 4.6: TF maps clustered with the most used clustering algorithms.

4.5 Dimensionality Reduction for Data Visualization

While the cross-correlation clustering algorithms provide a powerful method for the quantitative separation of signals, a complete diagnostic analysis also requires a qualitative interpretation of the results. The clustering algorithm provides a mathematical answer, partitioning the dataset into distinct groups, but it is through visualization that is possible validate, interpret, and effectively communicate the physical meaning of that separation. It allows an expert to visually confirm that the identified clusters are coherent and correspond to physically plausible phenomena. However, a fundamental challenge remains. To visualize the results, it is necessary to select specific features (e.g., amplitude, mean value, energy, zero-crossing rate) and represent them through two or three dimensional plots in order to examine their distribution. Although the feature space may be defined in a generic n dimensional domain, graphical representation constrains the analysis to two or three dimensions. Consequently, the complete informational content of the dataset and the associated feature set cannot be fully explored. Dimensionality reduction techniques are therefore essential tools to address this challenge [86, 87]. Their purpose is to transform a high dimensional space into a low dimensional representation (typically 2D or 3D) that can be easily visualized, while still preserving the intrinsic structure and salient characteristics of the original dataset. A comparative analysis of these methods reveals different strengths and trade-offs. In the the literature, a distinction is made between linear and nonlinear techniques. The former, such as Principal Component Analysis (PCA), are computationally efficient and offer a high degree of interpretability. PCA identifies the orthogonal directions (the principal components) that capture the maximum variance in the dataset, effectively summarizing the most significant features of the dataset [88, 89]. However, their underlying assumption of linearity means they may fail to capture more complex, non-linear structures present in the PD data. To address this, non-linear methods provide greater flexibility. t-distributed Stochastic Neighbor Embedding (t-SNE) is a technique designed specifically for visualization that excels at preserving the local structure of the data [90]. It is highly effective at revealing distinct clusters that might be hidden in the original high dimensional space, making it an excellent tool for exploratory analysis. Autoencoders, a class of artificial neural networks, represent another powerful non-linear approach [91, 92]. They learn to compress (encode) the input data into a low dimensional latent space and then reconstruct (decode) them, capturing complex data structures through their non-linear activation functions. In conclusion, the choice of a dimensionality reduction technique can be useful for a comprehensive PD analysis. While feature extraction methods like the TF Map provide a valuable and interpretable view, more general techniques such as PCA, t-SNE, and Autoencoders offer powerful alternatives for exploring the full complexity of the waveform data, validating separation algorithms, and gaining a deeper understanding of the underlying physical phenomena.

Chapter 5

Investigating the Interaction between Electric Field and Partial Discharges under Operating Conditions

5.1 Introduction

The previous chapters established the methodologies required to accurately measure and analyze space charge dynamics and PD phenomena in HVDC cables. In this chapter, these tools are applied to investigate the central hypothesis of this thesis: the accumulation of space charge and electric field inversion are a primary driver of PD inception and evolution under operating conditions. Understanding this relationship is paramount, as their combined effect can lead to accelerated insulation degradation and unpredictable service failures, representing a significant risk to the reliability of HVDC transmission systems. To demonstrate this interaction, two key experimental investigations have been conducted and illustrated in the following sections. The first study aims to isolate the effect of thermal gradients on PD activity, demonstrating how temperature induced changes in conductivity can alter the electric field distribution and intensify discharges without any change in the applied voltage. This experiment has been carried out to confirm the underlying physical mechanism in a controlled environment. Building upon this principle, the second experiment involves the simultaneous measurement of space charge and PD on a loaded HVDC model cable. This provides direct, time resolved evidence correlating the dynamics of electric field inversion with the onset of PD activity, thereby establishing a clear causal link between the two phenomena. The success of these investigations depends on the application of the custom developed diagnostic tools

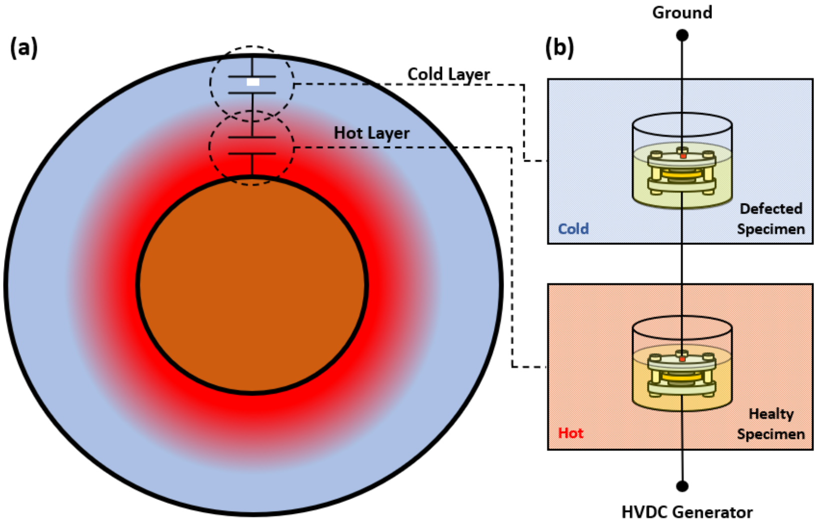

Figure 5.1: (a) Cross section of a cable with a thermal gradient and an air void defect. (b) Laboratory setup consisting of two specimens connected in series and immersed in separate oil tanks at different temperatures.

detailed previously: the high resolution PEA system for accurate field profiling and the cross-correlation clustering algorithm for the unambiguous identification of internal PD signals. Both tests have been carried out in the high voltage laboratory at the University of Palermo.

5.2 Influence of Thermal Gradients on PD Activity

The experimental setup, schematically illustrated in Fig. 5.1, has been designed as a simplified physical analogue of the complex electro-thermal phenomena occurring within the insulation of a loaded HVDC cable. The concept is to discretize the continuous thermal and conductivity gradient that develops across the insulation into two distinct, manageable layers. As shown in the diagram, the heated, healthy specimen represents the Hot Layer of the insulation, i.e., the hotter and more conductive region located closer to the conductor. Conversely, the defective specimen, containing an internal air void, represents the Cold Layer, corresponding to the cooler and less conductive region closer to the outer semiconductive screen. When the Hot Layer is heated, its conductivity increases and its resistivity decreases. In a series DC configuration, this leads to a redistribution of the applied voltage, resulting in a higher voltage drop, and therefore stronger electric field stress, across the Cold Layer, where the defect is located. This arrangement enables a clear demonstration of a fundamental principle: a change in conductivity in one region of the insulation directly affects the electrical stress experienced by another region, which is precisely the mechanism that can initiate PD in a real loaded cable. To reproduce this effect, the healthy specimen has been immersed in a

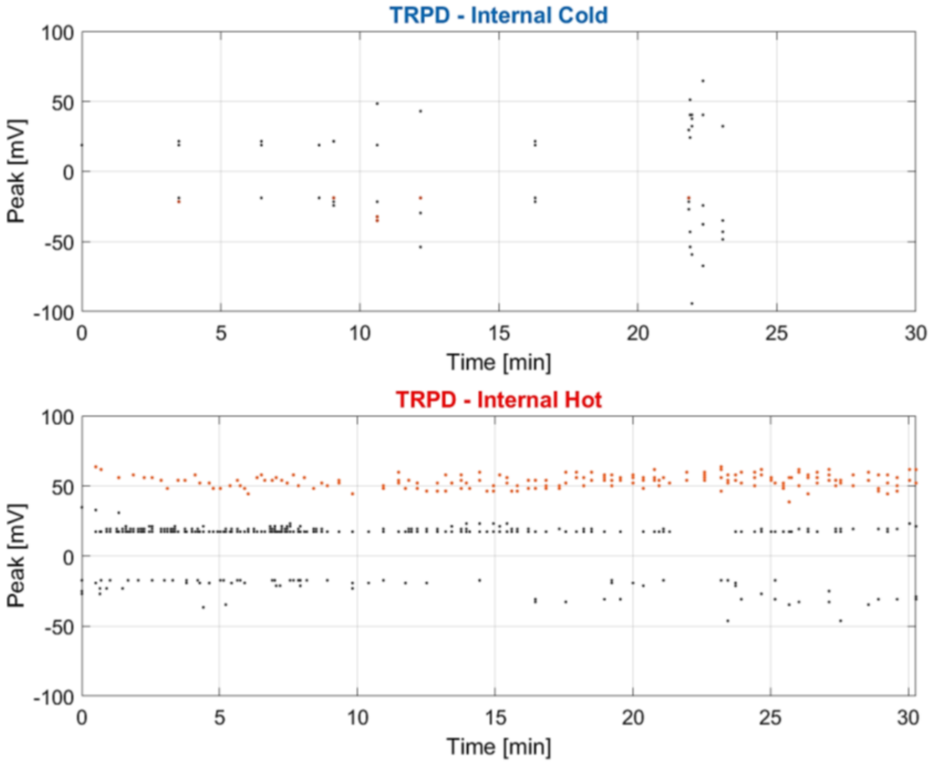

Figure 5.2: Time-Resolved Partial Discharge (TRPD) patterns of the acquired discharges. The PDs are highlighted in orange. The upper plot corresponds to the reference test with both specimens at room temperature (cold case), while the lower plot refers to the test with the healthy specimen heated to 80°C, establishing a thermal gradient (hot case).

temperature controlled oil bath and heated to 80°C, while the defective specimen has been kept at room temperature. A DC voltage of 20 kV has been applied to the two specimens connected in series. The measurement procedure consisted of two steps: a reference test with both specimens at room temperature (the cold case), followed by a test with the healthy specimen heated to 80°C to establish a thermal gradient (the hot case). Discharges have been detected using the Prycam, placed at the ground connection of the defective sample. The acquired discharges have been then separated using the algorithms described in Chapter 4. The results, reported in the TRPD patterns of Fig. 5.2, clearly highlight the impact of the thermal gradient. The discharges, marked in orange in the TRPD representation, show a significant increase when moving from the cold to the hot case: the number of internal discharges increase from fewer than a dozen to nearly 200, while their average amplitude approximately doubled. These findings demonstrate that thermal gradients, by altering the resistive field distribution, can act as a primary factor in intensifying PD activity, even under constant DC supply conditions.

5.3 Simultaneous PEA and PD Measurement on a Loaded Model Cable

To provide direct evidence of the link between space charge induced field changes and PD inception, a final experiment have designed to measure both phenomena simultaneously on a single HVDC model cable. This approach allows for a direct, time resolved correlation between the evolving electric field profile and the corresponding PD activity. In the tested cable, with a 5 mm insulation thickness, a well defined artificial air void defect (2 mm in diameter, 1 mm deep) was introduced at the outer dielectric-semicon interface to serve as a predictable PD source. The experimental setup integrated the two measurement systems developed in this thesis. The PEA measurement system has been positioned on a healthy, defect free section of the cable to monitor the space charge distribution, while a PryCam Wings sensor has been placed directly over the defect to detect any emitted PD signals. This choice is linked to the fact that air acts as an acoustic barrier and therefore direct measurement of the space charge in the defective section is impossible. A photo of the complete setup is shown in Fig. 5.3. Before the test, the cable has pre conditioned using a loading transformer to establish a stable thermal steady state with a 11°C gradient across the insulation (46.5°C on the conductor and 35.5°C on the outer semiconductive layer). Starting from the induced current value, the conductor temperature value has obtained using a thermal model implemented in a Finite Element Method (FEM) software. The thermal steady state condition has been reached after approximately 60 minutes. Excluding the pre conditioning phase, the effective duration of the test has been 40 minutes. The applied DC stress has been chosen equal to 80 kV. During the first 30 minutes, simultaneous measurements of space charge and partial discharges have been carried out, while in the final 10 minutes the induced current have been set to zero and only PD measurements have been performed. This current interruption triggered a thermal transient that altered the acoustic properties of the insulation, thereby affecting the transmission characteristics of the acoustic wave. It is important to note that the signal correction and calibration procedure described in Section 2.3 is specifically designed for a given thermal gradient, and therefore its validity may be compromised under transient thermal conditions. The following subsections report the results of the two measurements.

Figure 5.3: The arranged measurement setup for the simultaneous detection of space charge and PD in a DC model cable under operating conditions.

5.3.1 PEA Measurement Results

The analysis of the space charge profiles, acquired every 30 seconds, revealed a profound and dynamic evolution of the electric field distribution within the healthy section of cable's insulation. The most significant finding was the complete inversion of the electric field profile, which occurred approximately 10 minutes after the 80 kV DC voltage was applied.

As shown in Fig. 5.4, the initially Laplacian profile, which concentrates the maximum electric stress at the inner radius near the conductor, gradually transformed into an inverted profile. In this new steady state condition, the region of maximum electric stress shifted to the outer radius of the insulation, precisely where the artificial defect was located. Fig. 5.5 shows the electric field profiles acquired at 10 minute intervals from the beginning of the measurement up to 30 minutes. It can be clearly observed that the inversion process reaches a stable condition after approximately 10 minutes, since the profiles at 20 and 30 minutes are almost perfectly superimposed on the 10 minute profile. To monitor the temporal evolution

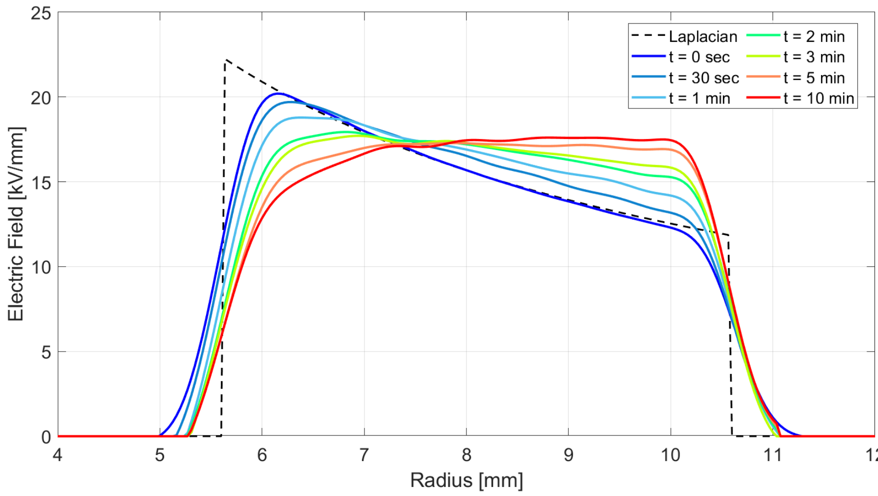

Figure 5.4: Electric field profiles during the first 10 minutes of the simultaneous measurement.

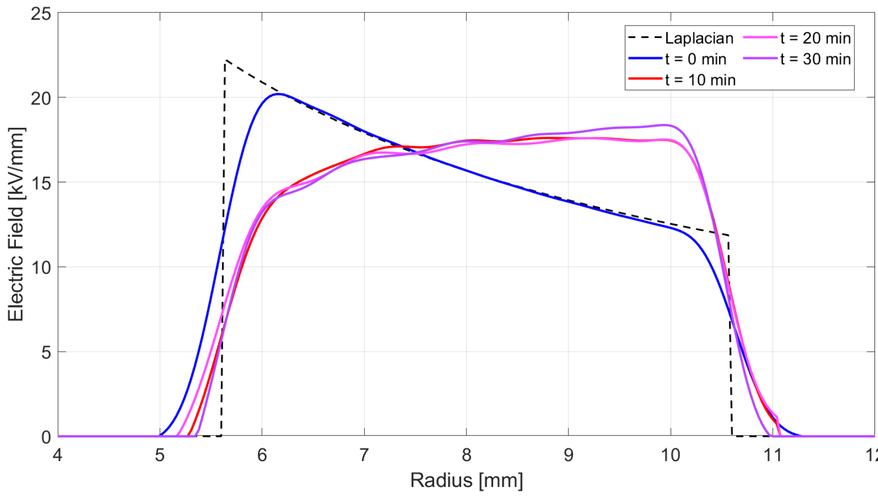

Figure 5.5: Electric field profiles during the first 30 minutes of the simultaneous measurement.

of the electric field in the outer region of the dielectric, the maximum value was extracted for each acquired profile in the 1 mm space immediately adjacent to the outer dielectric/semicon interface. The trend detected is shown in Fig 5.6. This redistribution of stress was not trivial, the electric field strength increased from an initial calculated value of 12 kV/mm to a peak value of 17 kV/mm once the inversion process was complete. This 41.6% increase in local stress demonstrates how space charge accumulation, driven by the combined electrical and thermal stresses, fundamentally alters the dielectric behavior of the insulation.

5.3.2 PD Measurement Results

The results from the PD measurement provided the second half of the evidence needed to establish the link between the two phenomena. The acquired data were analyzed in the post-processing phase using the cross-correlation-based clustering algorithm described in Chapter

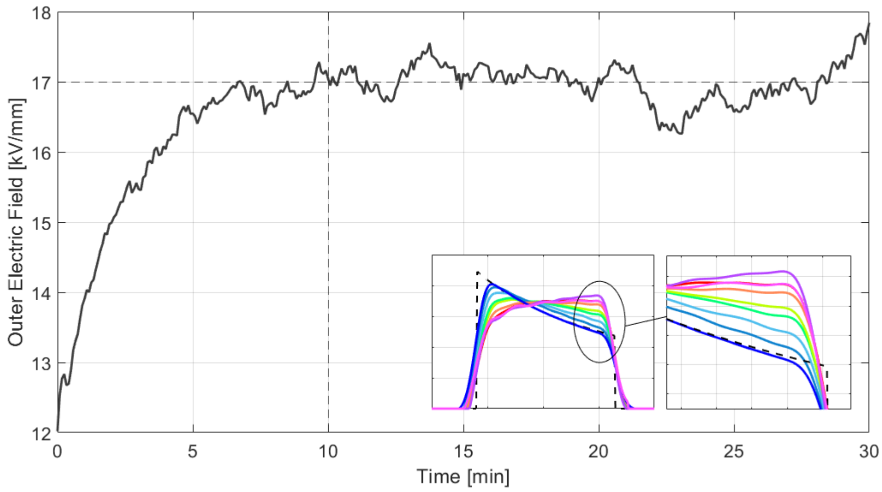

Figure 5.6: Maximum electric field values detected in the external cable insulating layer from 0 to 30 minutes.

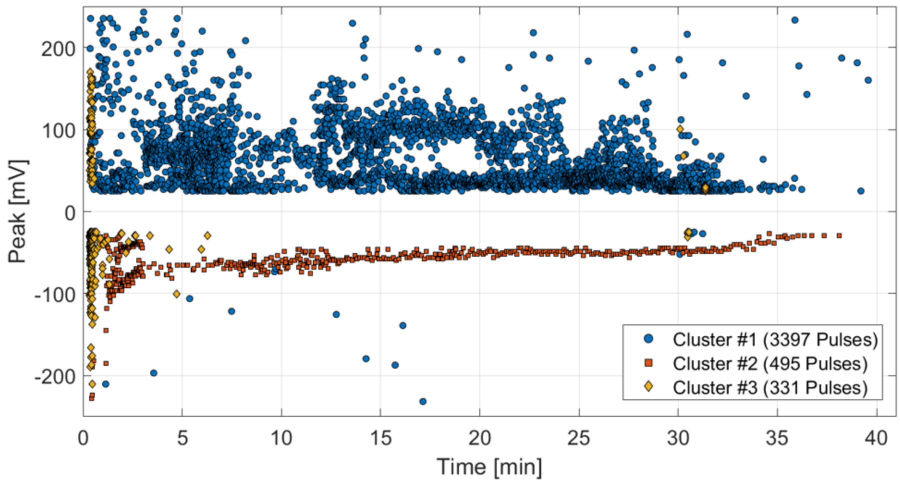

Figure 5.7: Clustered TRPD pattern for the PD dataset acquired during the entire simultaneous measurement.

4, allowing four different phenomena to be clearly distinguished. One of these was associated with the pulse generated by the PEA pulse generator for the production of the acoustic wave: since this signal was characterized by a constant amplitude that was significantly higher than that of all other events, its identification and subsequent elimination was immediate. The remaining three phenomena, on the other hand, were correctly separated and represented in the TRPD pattern shown in Fig. 5.7. Fig. 5.8 shows some representative examples of waveforms and corresponding frequency spectra for the three phenomena identified. It can be seen that the phenomenon highlighted in blue has a predominantly low-frequency content, while the one in orange is concentrated around 40 MHz (peak on 33 MHz). Finally, the phenomenon in yellow shows a spectrum characterized by intermediate components, thus placing it between the two previous cases. The TRPD pattern shows that the phenomenon in

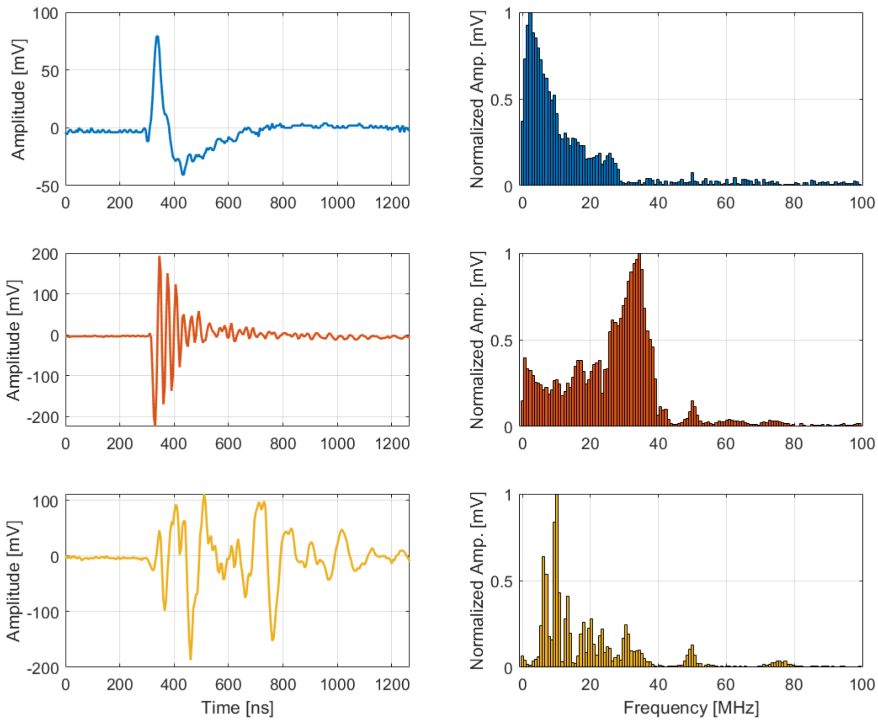

Figure 5.8: Detected pulses (on the left) and the related frequency spectrum (on the right) of the three different cluster.

yellow has a higher density of occurrence in the first few seconds of the test, and is therefore associated with the signals generated during the phase of increasing applied voltage (0–80 kV). The phenomenon in blue, on the other hand, shows a waveform and strong amplitude variability, characteristics typical of corona discharges. More peculiar is the behaviour of the orange phenomenon, of which 495 occurrences were recorded: it initially has very high amplitudes, followed by a progressive downward trend during the measurement. This behaviour makes it the most plausible candidate for internal discharges originating inside the artificial cavity of the cable.

5.3.3 Results Comparison

The direct correlation between the electric field dynamics and the PD activity is summarized in the plot shown in Fig. 5.9. This figure combines the temporal evolution of the electric field at the outer radius of the insulation, the location of the artificial defect, with the peak amplitude of the detected PDs over the 40 minute test period. At the application of the 80 kV voltage, the field begins to rise from its initial Laplacian value as the space charge accumulates and the field inversion process starts. After approximately 10 minutes, the field reaches a stable value, oscillating around a mean of 17 kV/mm. This field stabilization phase persists until the 30 minute mark, when the heating current is turned off. The subsequent thermal transient disrupts this equilibrium, causing the field to decay, entering in a not steady state condition. The bottom graph plots the peak amplitude of the detected PDs. PD were initiated approximately one minute after reaching the test voltage, corresponding to an electric field in the healthy section of the dielectric equal to 12.6 kV/mm, defined as the Partial Discharge Inception Electric Field (PDIEF). It should be noted that the electric field inside the cavity is necessarily higher due to the different permittivities of air and XLPE. The obtained value is consistent with previous experimental and simulation studies: in a FEM-based analysis carried out with COMSOL, a PDIEF of 17.95 kV/mm was estimated inside the cavity, while the corresponding value in the healthy dielectric region ranged between 12 and 13 kV/mm [93]. After inception, the discharge amplitude decreased and reached a stable average value of about –50 mV after approximately ten minutes, coinciding with the stabilization of the electric field profile. During the very first stage of the measurement, characterized by a high temporal gradient of the field (dE/dt), the inception and large amplitude of PD were influenced by both this parameter and the time constant τ associated with the cavity charging process. As the measurement progressed and the field stabilized, the contribution of dE/dt vanished, leaving the discharge activity governed solely by τ. Under steady thermal conditions, this parameter determines a constant Partial Discharge Repetition Rate (PDRR). As shown in Fig. 5.10, after about 15 minutes from the beginning of the test, the PDRR stabilized at approximately 10 discharges per minute. At the thirtieth minute, the load current was set to zero, triggering a thermal cooling transient in the cable. This process led to changes in the electric field, which tended to return toward a Laplacian distribution, and to an increase in the time constant τ. These effects caused a progressive reduction of the discharge activity, until its complete extinction at around the thirty-eighth minute. This plot provides a clear and compelling visual confirmation of the thesis's central hypothesis. The partial discharges are not simply present; their inception, sustained activity, and eventual extinction are directly governed by the local electric field at the site of the defect. The discharges ignite only when the space charge-induced field exceeds the inception threshold and are extinguished when the field falls below this critical value, demonstrating a direct causal link between space charge dynamics and PD phenomena.

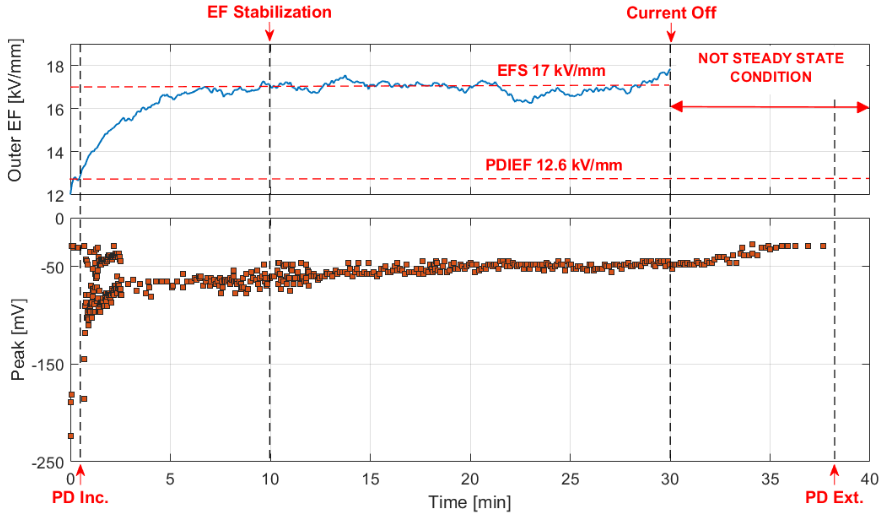

Figure 5.9: Electric field calculated in the healthy cable section and PD activity detected within the air void defect.

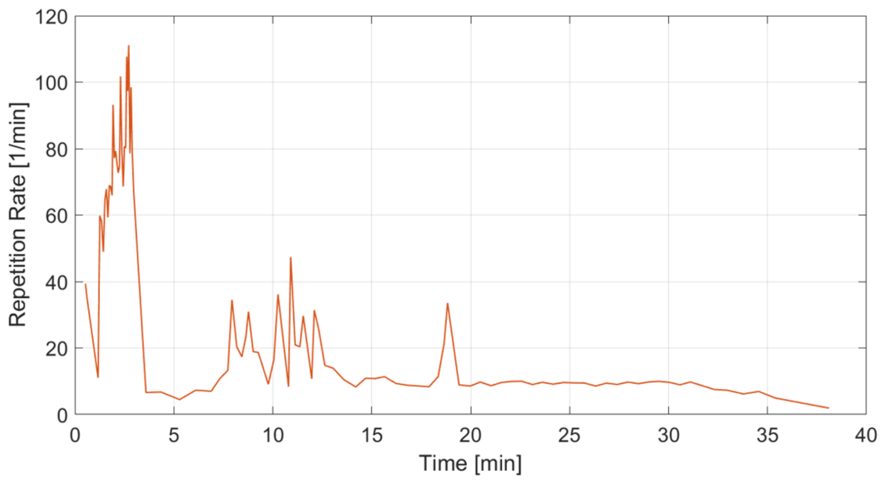

Figure 5.10: PD repetition rate over time.

Chapter 6

Conclusions and Future Work

6.1 Summary of Contributions

The research presented in this thesis has provided significant contributions to the understanding and diagnosis of critical aging phenomena in HVDC cable insulation systems. The main original contributions of this work are summarized as follows:

Development of Codes for PEA Profile Acquisition and Processing: In support of the PEA cell developed at the L.E.PR.E. laboratory, dedicated software have been implemented for both the control of the acquisition system and the subsequent processing of the profiles. The code integrates all the necessary steps to obtain and evaluate a reliable electric field profile. Special attention have been given to deconvolution techniques, considered the key element of the process. Several approaches reported in the literature have been therefore studied and implemented to enable a direct comparison.

A Novel Statistical Methodology for Electric Field Stabilization Assessment: This thesis introduced and validated a new statistical framework for evaluating the stabilization of the electric field in HVDC cables. By leveraging high frequency PEA measurements and analyzing the temporal evolution of statistical descriptors, this method has been demonstrated to be more robust and efficient than the standard spot-check approach prescribed by IEEE 1732. The methodology allows for an earlier and more reliable identification of stabilization, offering the potential to optimize industrial qualification testing protocols without compromising the accuracy of the assessment.

Advanced PD Separation Algorithm based on Cross-Correlation: An innovative clustering algorithm has been developed, which utilizes waveform similarity, quantified by the cross-correlation coefficient, as its primary metric. This approach has proven to be superior to traditional clustering methods that rely on feature space distance. The algorithm successfully separates different PD phenomena even when their patterns are overlapping, have diverse shapes, or varying densities, thus overcoming a key limitation in DC partial discharge analysis.

Experimental Proof of the Interaction between Space Charge and PDs: This research provided the first direct, quantitative experimental evidence of the causal link between space charge dynamics and partial discharge inception. Through simultaneous measurements, it was conclusively demonstrated that the triggering of PDs is not governed by the applied voltage level itself, but by the localized stress enhancement created by the space charge-induced electric field inversion. This finding confirms the central hypothesis that these two phenomena are part of a single, interconnected degradation process in HVDC insulation.

In addition to the technical developments and scientific findings summarized above, the outcomes of this research have been widely disseminated to the scientific community. The methodologies, experimental validations, and analytical evaluations were presented at leading international conferences where they received recognition and constructive feedback from experts in the field. Furthermore, several parts of this work have been published in peer-reviewed journals.

6.2 Overall Conclusion

The experimental results have validated the core hypothesis that PDs and space charge are not isolated phenomena but are instead components of a process that governs the aging of the insulation. It has been shown that a comprehensive and reliable assessment of HVDC cable performance requires an approach that considers this interplay. The development and application of the advanced diagnostic tools and data analysis methodologies presented in this research, from the robust statistical evaluation of field stabilization to the accurate separation of PD sources, represent a significant step forward in achieving this goal. The findings underscore that a deep understanding of these complex, time dependent phenomena is essential for the future design, testing, and monitoring of reliable HVDC power transmission systems.

6.3 Future Work

The conclusions of this research open several promising avenues for future investigation. The following directions are proposed to build upon the findings of this thesis. The extension of the simultaneous measurement methodology to a wider range of insulation materials, including both thermoplastic and thermoset compounds, and to different types and geometries of artificial defects, in order to generalize the findings and better understand how material properties influence the interaction between space charge and PDs. The development of real time monitoring systems by integrating the computationally efficient sequential PD clustering algorithm with the statistical framework for field analysis, enabling online diagnostics during factory acceptance tests or even in service operation and enabling the way for predictive maintenance strategies. The investigation of long term aging effects through accelerated campaigns, continuously monitoring the interaction between space charge and PDs to gather critical data on how this relationship evolves with material degradation and the application of advanced machine learning techniques, exploiting the combined datasets of space charge profiles and PDs patterns generated in this work to train deep learning models capable of automatically identifying complex patterns and predicting cable lifetime or failure probability.

Acknowledgements

I would like to express my deepest gratitude to my supervisor, Prof. Pietro Romano, for believing in me and welcoming me into his research group. His expertise, guidance, and generosity in sharing knowledge have inspired me and instilled a profound passion for research. His invaluable suggestions and advice have been instrumental in the completion of this work. I am also sincerely grateful to Ing. Antonino Imburgia for his essential support throughout all the activities conducted over the past three years. I owe both of them the chance to attend several international conferences. Those moments represented a unique opportunity to grow scientifically and to experience the international research community first-hand.

I would like to thank Prof. Guido Ala for his scientific support. His experience and valuable advice helped me conduct analyses with the necessary rigour and clarity.

My thanks go to all the professors of the doctoral committee, coordinated by Prof. Eleonora Riva Sanseverino, for providing a highly enriching PhD experience. The quality of my training was undoubtedly enhanced by their excellent organization and support.

I would like to acknowledge the EOSS staff, in particular Ing. Giuseppe Rizzo, Ing. Vincenzo Li Vigni, and Ing. Roberto Candela, for their invaluable guidance, continuous support, and the opportunities they provided for my professional growth.

I am grateful to the Prysmian staff, especially Ing. Marco Albertini, Ing. Grazia Berardi, and Ing. Stefano Franchi Bononi, for giving me the chance to visit several laboratories and gain first-hand insight into the industrial environment that complements research.

I would also like to thank the DEIS community for the outstanding organization of the international conferences I had the honor to attend. It was truly inspiring to meet in person the authors of books and articles fundamental to my research, an experience that enriched me both scientifically and personally.

Special thanks go to my friends, Roberto and Salvatore, for the joyful and carefree evenings, always invaluable in breaking the weekly routine.

I am especially grateful to my girlfriend, Floreana, for being by my side in moments of both joy and challenge throughout this journey.

Last but not least, I would like to thank my family: my father Baldo, my mother Vania, and my sister Simona, to whom I owe everything I am today.

Finally, I would like to thank you, dear reader, for the time and attention you have devoted to this work.

Bibliography

[1] F. Sioshansi, *Evolution of Global Electricity Markets: New paradigms, new challenges, new approaches*. Academic Press, 2013.

[2] J. Arrillaga, *High voltage direct current transmission*. No. 29, Iet, 1998.

[3] D. Jovcic, *High voltage direct current transmission: converters, systems and DC grids*. John Wiley & Sons, 2019.

[4] A. Deb and M. Naskar, "Recyclable polymeric cable insulation materials: A comprehensive review," *Power Research-A Journal of CPRI*, pp. 113–122, 2024.

[5] G. Mazzanti and M. Marzinotto, *Extruded cables for high-voltage direct-current transmission: advances in research and development*. John Wiley & Sons, 2013.

[6] D. Kind and H. Kärner, *High-voltage insulation technology*, vol. 621. Springer, 1985.

[7] L. A. Dissado and J. C. Fothergill, *Electrical degradation and breakdown in polymers*, vol. 9. Iet, 1992.

[8] B. Du, *Polymer insulation applied for HVDC transmission*. Springer Nature, 2020.

[9] I. Standard, "High-voltage test techniques: partial discharge measurements," *IEC-60270*, pp. 13–31, 2000.

[10] F. H. Kreuger, *Partial discharge detection in high-voltage equipment*. 1989.

[11] T. Tanaka and A. Greenwood, "Advanced power cable technology," tech. rep., Central Res. Inst. of Electric Power Research, Tokyo, 1983.

[12] G. Chen, M. Hao, Z. Xu, A. Vaughan, J. Cao, and H. Wang, "Review of high voltage direct current cables," *CSEE Journal of Power and Energy Systems*, vol. 1, no. 2, pp. 9–21, 2015.

[13] M. Florkowski, B. Florkowska, and R. W lodek, “Interaction of coupled thermal effect and space charge in hvdc cables,” *Energies*, vol. 18, no. 9, p. 2206, 2025.

[14] M. Samet, A. Kallel, and A. Serghei, “Maxwell-wagner-sillars interfacial polarization in dielectric spectra of composite materials: Scaling laws and applications,” *Journal of Composite Materials*, vol. 56, no. 20, pp. 3197–3217, 2022.

[15] T. T. N. Vu, G. Teyssedre, S. Le Roy, and C. Laurent, “Maxwell–wagner effect in multi-layered dielectrics: interfacial charge measurement and modelling,” *Technologies*, vol. 5, no. 2, p. 27, 2017.

[16] A. K. Upadhyay and C. C. Reddy, “Comparative study of famous conductivity models for low density polyethylene,” in *2017 IEEE International Conference on Industrial and Information Systems (ICIIS)*, pp. 1–4, 2017.

[17] Z. Xing, C. Zhang, H. Cui, Y. Hai, Q. Wu, and D. Min, “Space charge accumulation and decay in dielectric materials with dual discrete traps,” *Applied Sciences*, vol. 9, no. 20, p. 4253, 2019.

[18] M. Rafiq and M. H. Zink, “Understanding the space charge dynamics and its impact on insulation degradation in power transformers: A critical review,” *Electric Power Systems Research*, vol. 245, p. 111644, 2025.

[19] Y. Liu, H. Liu, L. Yu, Y. Li, and L. Gao, “Effect of thermal stress on the space charge distribution of 160 kv hvdc cable insulation material,” *IEEE Transactions on Dielectrics and Electrical Insulation*, vol. 24, no. 3, pp. 1355–1364, 2017.

[20] Y. Li, M. Yasuda, and T. Takada, “Pulsed electroacoustic method for measurement of charge accumulation in solid dielectrics,” *IEEE transactions on Dielectrics and Electrical Insulation*, vol. 1, no. 2, pp. 188–195, 1994.

[21] A. Imburgia, R. Miceli, E. R. Sanseverino, P. Romano, and F. Viola, “Review of space charge measurement systems: acoustic, thermal and optical methods,” *IEEE Transactions on Dielectrics and Electrical Insulation*, vol. 23, no. 5, pp. 3126–3142, 2016.

[22] A. Imburgia, P. Romano, G. Chen, G. Rizzo, E. Riva Sanseverino, F. Viola, and G. Ala, “The industrial applicability of pea space charge measurements, for performance optimization of hvdc power cables,” *Energies*, vol. 12, no. 21, p. 4186, 2019.

[23] H. Ghorbani, A. Abbasi, M. Jeroense, A. Gustafsson, and M. Saltzer, "Electrical characterization of extruded dc cable insulation—the challenge of scaling," *IEEE Transactions on Dielectrics and Electrical Insulation*, vol. 24, no. 3, pp. 1465–1475, 2017.

[24] N. Hozumi, "Space charge measurement techniques for practical insulation systems," in *2023 IEEE 4th International Conference on Electrical Materials and Power Equipment (ICEMPE)*, pp. 1–8, IEEE, 2023.

[25] S. Morita, N. Fuse, T. Takahashi, T. Takahashi, S. Zahra, and N. Hozumi, "Space charge measurement of 23-mm-thick xlpe cable at ambient and high temperatures," *IEEE Transactions on Dielectrics and Electrical Insulation*, vol. 29, no. 4, pp. 1491–1497, 2022.

[26] G. Rizzo, P. Romano, A. Imburgia, and G. Ala, "Review of the pea method for space charge measurements on hvdc cables and mini-cables," *Energies*, vol. 12, no. 18, p. 3512, 2019.

[27] S. Zahra, S. Morita, M. Utagawa, T. Kawashima, Y. Murakami, N. Hozumi, P. Morshuis, Y.-I. Cho, and Y.-H. Kim, "Space charge measurement equipment for full-scale hvdc cables using electrically insulating polymeric acoustic coupler," *IEEE Transactions on Dielectrics and Electrical Insulation*, vol. 29, no. 3, pp. 1053–1061, 2022.

[28] S. Zahra, T. Kawashima, Y. Murakami, and N. Hozumi, "Small-size space charge measurement device for power cables by using electrically insulated acoustic coupler," in *2020 IEEE 3rd International Conference on Dielectrics (ICD)*, pp. 359–362, 2020.

[29] M. Fu, G. Chen, A. Davies, and J. Head, "Space charge measurements in cables using the pea method:-signal data processing considerations," in *ICSD'01. Proceedings of the 20001 IEEE 7th International Conference on Solid Dielectrics (Cat. No. 01CH37117)*, pp. 219–222, IEEE, 2001.

[30] A. Vazquez, G. Chen, A. Davies, and R. Bosch, "Space charge measurement using pulsed electroacoustic technique and signal recovery," *Journal of the European Ceramic Society*, vol. 19, no. 6-7, pp. 1219–1222, 1999.

[31] L. H. Pearson, J. R. Dennison, E. W. Griffiths, and A. C. Pearson, "Pea system modeling and signal processing for measurement of volume charge distributions in thin dielectric films," *IEEE Transactions on Plasma Science*, vol. 45, no. 8, pp. 1955–1964, 2016.

[32] T. Fechner, Y. Zhou, X. Lei, and M. Zhou, “Important design aspects of pulsed electroacoustic measurement systems for thick full-size cable specimen,” in *2018 International Conference on Power System Technology (POWERCON)*, pp. 3960–3966, IEEE, 2018.

[33] M. Fu and G. Chen, “Space charge measurement in polymer insulated power cables using flat ground electrode pea system,” *IEE Proceedings-Science, Measurement and Technology*, vol. 150, no. 2, pp. 89–96, 2003.

[34] B. Vissouvanadin, C. Laurent, S. Le Roy, G. Teyssèdre, I. Denizet, M. Mammeri, and B. Poisson, “A deconvolution technique for space charge recovery in lossy and dispersive dielectrics using pea method,” in *2010 Annual Report Conference on Electrical Insulation and Dielectic Phenomena*, pp. 1–4, IEEE, 2010.

[35] X. Li, Y. An, T. Kawashima, Y. Murakami, and N. Hozumi, “Transfer matrix for space-charge analysis of insulating systems with complex geometries,” in *2023 IEEE 4th International Conference on Electrical Materials and Power Equipment (ICEMPE)*, pp. 1–4, IEEE, 2023.

[36] T. T. N. Vu, L. Berquez, and G. Teyssedre, “Space charge measurement by electroacoustic method: impact of acoustic properties of materials on the response for different geometries,” *International Journal on Electrical Engineering and Informatics*, vol. 10, no. 4, pp. 631–647, 2018.

[37] T. Wendel, J. Kindersberger, M. Hering, and K. Juhre, “Space charge measurement in epoxy according to the pulsed electro acoustic method under consideration of attenuation and dispersion,” in *VDE High Voltage Technology 2018; ETG-Symposium*, pp. 1–6, VDE, 2018.

[38] H.-C. Jung, H.-G. Kim, T.-I. Choi, and S. Hwangbo, “Automatic measurement system of the space charge distribution by a two-step deconvolution,” *Journal of Electrical Engineering & Technology*, vol. 14, no. 5, pp. 2049–2055, 2019.

[39] D. Van der Born, “Investigation of space charge injection, conduction and trapping mechanisms in polymeric hvdc mini-cables,” 2011.

[40] R. Bodega, “Space charge accumulation in polymeric high voltage dc cable systems,” 2006.

[41] M. Fu, *Space charge measurement in polymer insulated power cables using the PEA method*. PhD thesis, University of Southampton, 2002.

[42] H. Zheng, *Application of PEA technique to space charge measurement in cylindrical geometry HV cable systems*. PhD thesis, University of Leicester, 2015.

[43] A. Di Fatta, G. Rizzo, P. Romano, G. Ala, and A. Imburgia, "A review and functional analysis of space charge measurement deconvolution techniques for hvdc cables," *IEEE Transactions on Dielectrics and Electrical Insulation*, 2025.

[44] R. Bracewell and P. B. Kahn, "The fourier transform and its applications," *American Journal of Physics*, vol. 34, no. 8, pp. 712–712, 1966.

[45] T. Maeno, T. Futami, H. Kushibe, T. Takada, and C. Cooke, "Measurement of spatial charge distribution in thick dielectrics using the pulsed electroacoustic method," *IEEE transactions on Electrical Insulation*, vol. 23, no. 3, pp. 433–439, 2002.

[46] G. Chen, Y. Chong, and M. Fu, "Calibration of the pulsed electroacoustic technique in the presence of trapped charge," *Measurement Science and Technology*, vol. 17, no. 7, p. 1974, 2006.

[47] M. J. P. Jeroense, "Charges and discharges in hvdc cables in particular in mass-impregnated hvdc cables.," 1998.

[48] K. Hencken and A. Abbasi, "Analysis of the deconvolution and reconstruction of pea signals for hv insulation materials," in *2016 IEEE International Conference on Dielectrics (ICD)*, vol. 2, pp. 926–929, IEEE, 2016.

[49] A. Gupta and C. C. Reddy, "Analytical insights into parameter estimation for wiener deconvolution," *IEEE Transactions on Instrumentation and Measurement*, vol. 66, no. 10, pp. 2566–2575, 2017.

[50] D. Potts and G. Steidl, "Preconditioners for ill-conditioned toeplitz matrices," *BIT Numerical Mathematics*, vol. 39, no. 3, pp. 513–533, 1999.

[51] A. N. Tikhonov *et al.*, "On the stability of inverse problems," in *Dokl. akad. nauk sssr*, vol. 39, pp. 195–198, 1943.

[52] A. Gupta and C. Reddy, "On the estimation of actual space charge using pulsed electro-acoustic system," *IEEE Transactions on Dielectrics and Electrical Insulation*, vol. 23, no. 5, pp. 3086–3093, 2016.

[53] P. C. Hansen, “Regularization tools: A matlab package for analysis and solution of discrete ill-posed problems,” *Numerical algorithms*, vol. 6, no. 1, pp. 1–35, 1994.

[54] P. C. Hansen, “Analysis of discrete ill-posed problems by means of the l-curve,” *SIAM review*, vol. 34, no. 4, pp. 561–580, 1992.

[55] A. Gupta and C. Reddy, “Sparse de-convolution of space charge signal in pea method,” in *2013 IEEE International Conference on Signal Processing, Computing and Control (ISPCC)*, pp. 1–4, IEEE, 2013.

[56] A. Gholami and M. D. Sacchi, “A fast and automatic sparse deconvolution in the presence of outliers,” *IEEE Transactions on geoscience and remote sensing*, vol. 50, no. 10, pp. 4105–4116, 2012.

[57] I. Selesnick, “Sparse deconvolution (an mm algorithm),” *Connexions*, pp. http–cnx, 2012.

[58] J. Zhao, Y. Ge, J. Chen, S. Wang, and K. Wu, “An improved space charge measurement approach for power cables,” *IEEE Transactions on Instrumentation and Measurement*, vol. 73, pp. 1–7, 2024.

[59] Y. An, X. Li, T. Kawashima, Y. Murakami, Y. Tanaka, and N. Hozumi, “Laplace deconvolution for improvement of signal processing in space charge measurement applied to full-scale cables,” *IEEE Transactions on Dielectrics and Electrical Insulation*, 2025.

[60] A. Yeongguk, X. Li, T. Kawashima, Y. Murakami, and N. Hozumi, “Signal processing for space charge measurement using laplace deconvolution,” in *2022 9th International Conference on Condition Monitoring and Diagnosis (CMD)*, pp. 811–814, IEEE, 2022.

[61] A. Imburgia, P. Romano, G. Rizzo, A. Di Fatta, G. Akbar, F. Viola, G. Berardi, M. Albertini, S. F. Bononi, and G. Ala, “Simulation of a new developed pea cell for flat specimens and full-size cables,” in *2023 IEEE Conference on Electrical Insulation and Dielectric Phenomena (CEIDP)*, pp. 1–4, IEEE, 2023.

[62] P. Romano, A. Imburgia, G. Rizzo, A. Di Fatta, G. Akbar, F. Viola, G. Berardi, M. Albertini, S. F. Bononi, and G. Ala, “Development of a new pea cell for model cables,” in *2023 IEEE Conference on Electrical Insulation and Dielectric Phenomena (CEIDP)*, pp. 1–4, IEEE, 2023.

[63] S. Zahra, S. Morita, M. Utagawa, T. Kawashima, Y. Murakami, N. Hozumi, P. Morshuis, Y.-I. Cho, and Y.-H. Kim, "Space charge measurement equipment for full-scale hvdc cables using electrically insulating polymeric acoustic coupler," *IEEE Transactions on Dielectrics and Electrical Insulation*, vol. 29, no. 3, pp. 1053–1061, 2022.

[64] H. Xiao, K. Sun, J. Pan, Y. Li, and Y. Liu, "Review of hybrid hvdc systems combining line communicated converter and voltage source converter," *International Journal of Electrical Power & Energy Systems*, vol. 129, p. 106713, 2021.

[65] G. Li, T. An, J. Liang, W. Liu, T. Joseph, J. Lu, M. Szechtman, B. R. Andersen, and Y. Lan, "Power reversal strategies for hybrid lcc/mmc hvdc systems," *CSEE Journal of Power and Energy Systems*, vol. 6, no. 1, pp. 203–212, 2020.

[66] Y. Zhou, B. Gao, W. Wang, and K. Song, "Influence of polarity reversal period and temperature gradient on space charge evolution and electric field distribution in hvdc extruded cable," *Energies*, vol. 15, no. 3, 2022.

[67] S. Wang, S. Luo, Y. Tu, C. Wang, and S. Qin, "Effect of polarity reversal on space charge properties of cb/ldpe composite under dc field," *IEEE transactions on Dielectrics and Electrical Insulation*, vol. 24, no. 3, pp. 1349–1354, 2017.

[68] Y. Tanaka, R. Kodera, T. Kato, H. Miyake, H. Mori, and Y. Yagi, "Observation of space charge accumulation in cable insulating materials at voltage polarity reversal," in *IEEE Int. Conf. Insulated Power Cables*, vol. 9, p. 1, 2015.

[69] G. Mazzanti, M. Marzinotto, J. Castellon, G. Chen, J. Fothergill, M. Fu, N. Hozumi, J.-H. Lee, J. Li, F. Mauseth, *et al.*, "Recommended practice for space charge measurements in high voltage direct current extruded cables for rated voltages up to 550 kv," 2017.

[70] G. Mazzanti, "Space charge measurements in high voltage dc extruded cables in ieee standard 1732," *IEEE Electrical Insulation Magazine*, vol. 33, no. 4, pp. 9–15, 2017.

[71] N. Pattanadech, R. Haller, S. Kornhuber, and M. Muhr, *Partial Discharges (PD): Detection, Identification and Localization*. John Wiley & Sons, 2023.

[72] G. Paoletti and A. Golubev, "Partial discharge theory and applications to electrical systems," in *Conference record of 1999 annual pulp and paper industry technical conference (Cat. No. 99CH36338)*, pp. 124–138, IEEE, 1999.

[73] M. Yaacob, M. A. Alsaedi, J. Rashed, A. Dakhil, and S. Atyah, "Review on partial discharge detection techniques related to high voltage power equipment using different sensors," *Photonic sensors*, vol. 4, no. 4, pp. 325–337, 2014.

[74] H. D. Ilkhechi and M. H. Samimi, "Applications of the acoustic method in partial discharge measurement: A review," *IEEE Transactions on Dielectrics and Electrical Insulation*, vol. 28, no. 1, pp. 42–51, 2021.

[75] H. Chai, B. T. Phung, and S. Mitchell, "Application of uhf sensors in power system equipment for partial discharge detection: A review," *Sensors*, vol. 19, no. 5, p. 1029, 2019.

[76] P. Romano, A. Imburgia, and G. Ala, "Partial discharge detection using a spherical electromagnetic sensor," *Sensors*, vol. 19, no. 5, p. 1014, 2019.

[77] R. Bartnikas, "Partial discharges. their mechanism, detection and measurement," *IEEE Transactions on dielectrics and electrical insulation*, vol. 9, no. 5, pp. 763–808, 2002.

[78] P. H. Morshuis and J. J. Smit, "Partial discharges at dc voltage: their mechanism, detection and analysis," *IEEE Transactions on dielectrics and electrical insulation*, vol. 12, no. 2, pp. 328–340, 2005.

[79] V. Dmitriev, R. M. Oliveira, R. F. Zampolo, P. R. Moutinho de Vilhena, F. de Souza Brasil, and M. F. Fernandes, "Partial discharges: Physics and classification," in *Partial Discharges in Hydroelectric Generators: Detection, Processing, Classification, and Pinpointing*, pp. 11–36, Springer, 2023.

[80] W. J. K. Raymond, H. A. Illias, H. Mokhlis, *et al.*, "Partial discharge classifications: Review of recent progress," *Measurement*, vol. 68, pp. 164–181, 2015.

[81] P. Romano, G. Presti, A. Imburgia, and R. Candela, "A new approach to partial discharge detection under dc voltage," *IEEE Electrical Insulation Magazine*, vol. 34, no. 4, pp. 32–41, 2018.

[82] M. Florkowski, "Classification of partial discharge images using deep convolutional neural networks," *Energies*, vol. 13, no. 20, p. 5496, 2020.

[83] J. Braasch, "Convolution, fourier analysis, cross-correlation and their interrelationship," in *Springer Handbook of Systematic Musicology*, pp. 273–284, Springer, 2018.

[84] A. Di Fatta, A. Imburgia, G. Rizzo, G. Akbar, V. L. Vigni, P. Romano, and G. Ala, "Modified hierarchical clustering algorithm for partial discharge separation," in *2023 IEEE Conference on Electrical Insulation and Dielectric Phenomena (CEIDP)*, pp. 1–4, IEEE, 2023.

[85] A. Imburgia, A. Di Fatta, P. Romano, G. Rizzo, V. L. Vigni, and G. Ala, "A study on partial discharges pattern recognition under dc voltage through clustering algorithms and cross correlation filter," *IEEE Transactions on Dielectrics and Electrical Insulation*, vol. 30, no. 6, pp. 2543–2550, 2023.

[86] C. O. S. Sorzano, J. Vargas, and A. P. Montano, "A survey of dimensionality reduction techniques," *arXiv preprint arXiv:1403.2877*, 2014.

[87] L. Van Der Maaten, E. O. Postma, H. J. Van Den Herik, *et al.*, "Dimensionality reduction: A comparative review," *Journal of machine learning research*, vol. 10, no. 66-71, p. 13, 2009.

[88] R. Liao, Y. Fernandess, K. Tavernier, G. Taylor, and M. Irving, "Recognition of partial discharge patterns," in *2012 IEEE power and energy society general meeting*, pp. 1–8, IEEE, 2012.

[89] K. Lai, B. Phung, and T. Blackburn, "Partial discharge analysis using pca and som," in *2007 IEEE Lausanne Power Tech*, pp. 2133–2138, IEEE, 2007.

[90] Y. Fu, K. Zhou, G. Zhu, Z. Li, Y. Li, P. Meng, Y. Xu, and L. Lu, "A partial discharge signal separation method applicable for various sensors based on time–frequency feature extraction of t-sne," *IEEE Transactions on Instrumentation and Measurement*, vol. 73, pp. 1–9, 2023.

[91] R. Zemouri, M. Levesque, N. Amyot, C. Hudon, O. Kokoko, and S. A. Tahan, "Deep convolutional variational autoencoder as a 2d-visualization tool for partial discharge source classification in hydrogenerators," *IEEE Access*, vol. 8, pp. 5438–5454, 2019.

[92] N.-D. T. Thi, T.-D. Do, J.-R. Jung, H. Jo, and Y.-H. Kim, "Anomaly detection for partial discharge in gas-insulated switchgears using autoencoder," *IEEE Access*, vol. 8, pp. 152248–152257, 2020.

[93] G. Rizzo, P. Romano, A. Imburgia, and G. Ala, “Partial discharges in hvdc cables-the effect of the temperature gradient during load transients,” *IEEE Transactions on Dielectrics and Electrical Insulation*, vol. 28, no. 5, pp. 1767–1774, 2021.

List of Figures